UNIVERSITY OF MIAMI

LOW DRAG AUTOMOTIVE MIRROR SIMULATION
USING PASSIVE JET FLOW CONTROL

By

Greg Woyczynski

A THESIS

Submitted to the Faculty
of the University of Miami
in partial fulfillment of the requirements for
the degree of Master of Science

Coral Gables, Florida

August 2014

UNIVERSITY OF MIAMI

A thesis submitted in partial fulfillment of
the requirements for the degree of
Master of Science

LOW DRAG AUTOMOTIVE MIRROR SIMULATION
USING PASSIVE JET FLOW CONTROL

Greg Woyczynski

Approved:

_____
Gecheng Zha, Ph.D.
Professor of Mechanical and
Aerospace Engineering

_____
Hongtan Liu, Ph.D.
Professor of Mechanical and
Aerospace Engineering

_____
Amir Rahmani, Ph.D.
Professor of Mechanical and
Aerospace Engineering

_____
M. Brian Blake, Ph.D.
Dean of the Graduate School

_____
Mike Brown, Ph.D.
Professor of Marine Physics

WOYCZYNSKI, GREG   (M.S., Mechanical Engineering)

<u>Low Drag Automotive Mirror Simulation Using Passive Flow Jet Control</u> (August 2014)

Abstract of a thesis at the University of Miami.

Thesis supervised by Professor Gecheng Zha.
No. of pages in text. (77)

The work presented in this thesis includes a detailed study of passive jet flow control as

applied to an automotive side-view mirror. Numerical analysis as well as experimental

prototype tests are conducted on three models of mirrors: one baseline model and two

others with variable jet strength. An open inlet draws a certain amount of flow, passes it

through a converging duct, and exhausts the flow as a jet with an angle toward the center

of the mirror. The jet forms a boat-tail effect that entrains high energy flow from the free

stream to the base area, increasing the base pressure, and reducing the base drag.

Throughout this thesis, drag reduction compared to the conventional automotive mirror is

proven and detailed through computational fluid dynamics (CFD) simulation validated

with wind tunnel experiments. The CFD algorithm employed is high order large eddy

simulation (LES) and the code is produced by the CFD research group at the University

of Miami. The jet 1 model has an inlet area that is 10% of the base area and is shown to

have a drag decrease of 29.41% in CFD. In the jet 2 model, which has a four times larger

inlet, we see a 40.91% drag decrease in CFD. This drag decrease is primarily due to

wake reduction. The jet is observed as pulsing into the base area. The jet pulsation on

the mid vertical and horizontal plane has a phase lag. The pulsing jet introduces coherent

structures that enhance the entrainment of the main flow to the base area. An interesting

phenomenon is observed that the jet generates negative entropy, which means the jet is energized by the free stream. The passive flow control is thus similar to an active jet flow control in this way. 1

The mechanism of the negative entropy is not fully understood yet at this stage; more study are needed. The following are some task that warrant investigation: LES with refined grid to resolve the wake better in order to match the experimental PIV measurements, study the effect of different jet flow angle, study the inlet and outlet ratio effect on the mixing and entrainment, and scaling for the drag reduction with the geometric parameters.

Acknowledgment

Contents

List of Figures

List of Tables

Chapter 1

Introduction

1.1 Background

Since the invention of the automobile there has always been concerns about safety.
Environmental safety, pedestrian safety and of course the safety of the people inside the
car. To keep the people inside the car safe, in 1960 the U.S. government realized that
regulations had to be made to increase the driver's awareness.
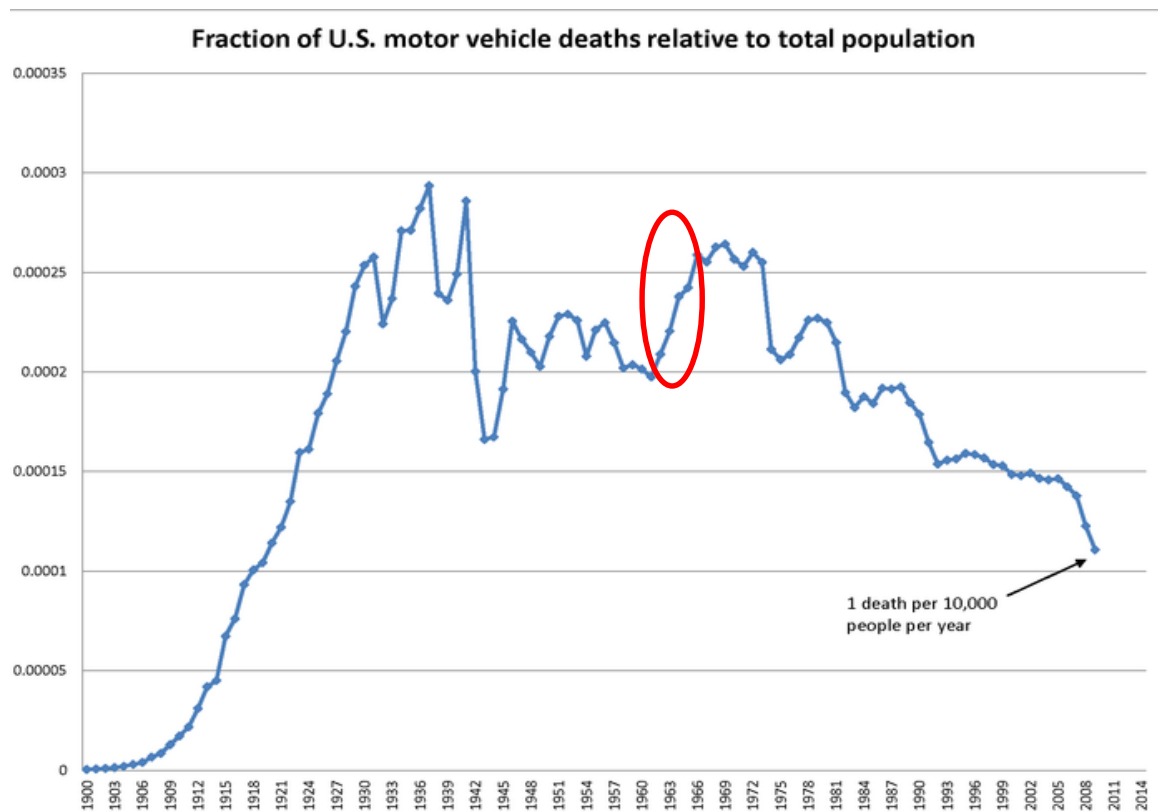
Fig. 1: U.S. Automobile Fatalities

With a rise in roads being built with four or more lanes, such as highways, the U.S.
Senate saw a need and passed Federal Motor Vehicle Safety Standard 111 on March 1,
1960. The increasing popularity of these large roads were creating a huge amount side-
impact collisions (mostly collisions caused by changing lanes). Standard 111 required all

cars to have an, " …outside mirror of unit magnification" [1]. These side view mirrors have successfully improved driver awareness and because of their wide implementation, learning how to use the side view mirrors is now a staple of any driving safety school.

Since 1960 many changes have been made in the world of automobiles. With increasing public concern on global climate change, reducing fuel consumption and controlling carbon emissions, a clean environment has become a top priority. The Environmental Protection Agency estimated that transportation byproducts made up 28% of United States greenhouse gas emissions in 2013 [2]. For the average automobile consumer, there is a growing list of concerns aside from those environmental concerns. The greatest of those concerns being cost of ownership. In reaction to consumer worries and rising fuel prices, cars have become smaller and smaller. As the body of the car becomes smaller the percentage of external surface area taken by the side view mirror increases.

There is a plethora of research going into side view cameras replacing mirrors, there are pros and cons inherent in these systems. Removing the side mirrors from the vehicle is the best way to reduce drag. However, this approach would require creating a system that fully replaces the functionality of the mirrors displaying a real-time feed. Although this system could largely replace the functionality of the mirrors, it fails to satisfy many parameters. The camera system could not serve as an immediate solution. Codes and standards would be violated because even if the camera system were installed, the U.S. National Highway Traffic Safety Administration still requires mirrors on the vehicles. Replacing conventional side-view mirrors with a camera system to view traffic,

pedestrians and objects around the vehicle would also involve a significant adjustment by all drivers who now rely on using side mirrors. Switching to a camera system requires additional training for all drivers not to mention an adaptation period as drivers become accustomed to operating a vehicle without the side mirrors. Although many vehicles currently have back-up camera systems installed, they primarily provide redundancy to the mirrors and are typically used in low-speed backing situations. Removal of the mirrors would negate the redundant safety advantage of cameras.

A camera system would also be expensive compared to side mirrors due to the sophisticated equipment and software that would have to be installed. It is clearly not the most economically viable option. This type of complex system may also rely on more sophisticated driver engagement at high speeds and prove to be distracting or difficult for many drivers. Compared to current mirror concepts, the potential for system failure is much higher. Too many parameters would be compromised using this approach.

For many types of automobiles, transportation fossil fuel is likely to remain as the dominant energy source in the foreseeable future due to its high energy density. A University of Michigan study (Fig. 2) predicts that the preponderance of such fuels will continue through 2040 [12].

US Energy Consumption by Fuel Source, 1949-2040
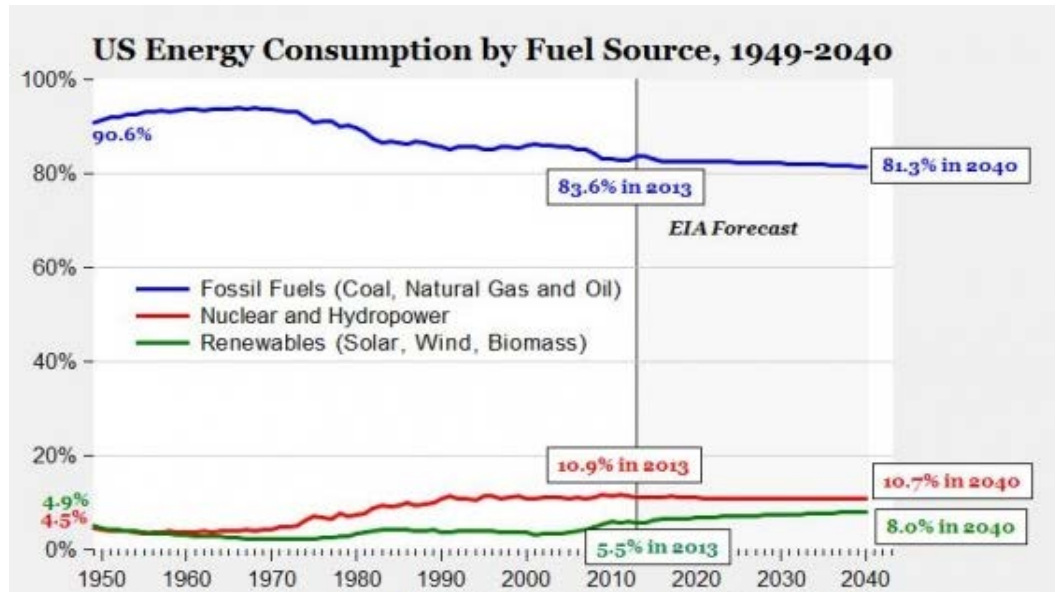
Fig. 2: U.S. Energy Consumption Forecast

The aerodynamic drag is a major hindrance that the propulsion system of the vehicle needs to overcome by consuming energy and fuel. Commercial automobiles have relatively high drag coefficients due to their blunt body shapes, which create high pressure drag due to base flow [3]. To clarify, the base region is the section of the fluid flow that is completely separated from the main flow . Due to the abrupt cut off of the solid wall surface, the flow loses energy in the base area significantly. This energy loss creates a base region where the momentum and pressure are very low. We have sufficient evidence to characterize this flow as base flow because we see many of its common characteristics such as vortex shedding, high turbulence intensity, high velocity fluctuation and low total pressure.

 Vortex shedding is basically a pattern of flow detachment. In any airfoil, flow separation often results in increased drag. For this reason extensive amounts of research,

this thesis included, has gone into the design of streamlined surfaces that delay separation and keep local flow attached for as long as possible [9]. In this case, pressure drag arises from the shape of the mirror. The general size and body shape are the most important factors. Bodies that have a larger cross-section perpendicular to the flow will have a higher pressure drag than slender bodies. The drag force increases with the square of velocity, so reducing this force becomes crucial, especially for higher velocity highway driving.

$$F_d = \frac{1}{2}\rho V^2 A_s \, C_D \qquad\qquad (\text{Eq. 1})$$

Common methods of drag reduction are mostly focused on lowering the drag coefficient, C_D , by creating more continuous streamlines and a reducing the boundary layer separation with its attendant vortices.

This new mirror design utilizes a drag reduction method using a passive flow control jet. This method was invented by Dr. Gecheng Zha in 2012 [4,5,6]. The mirror, with an open inlet, draws a certain amount of flow, passes it through a converging duct, and exhausts the flow as a jet with an angle towards the center of the mirror. The jet forms a boat-tail effect that entrains the high energy flow from the free stream to the base area, increasing the base pressure, and reducing the base drag. This new mirror concept with henceforth be known as "Jet Mirror" for simplicity. Also, throughout the paper there will be references made to the "front" and "back" of the mirror. The front and back as well as the length are labeled in Fig. 3. The external side-view mirrors create 2-7% total drag of a typical car, and can be even higher for large trucks [7]. The front curvature of conventional side mirrors is beneficial to reduce front stagnation area and thus pressure

drag but such a small object should not be responsible for such a large percentage of the drag.

Front

Length

129

126.18

Back

126.18

190.5
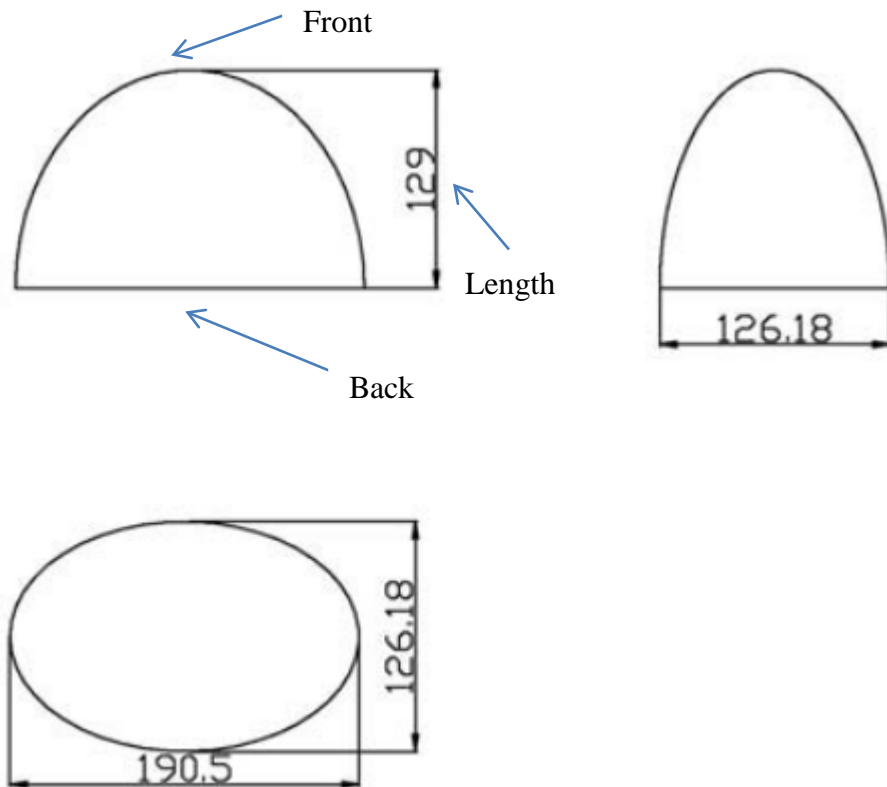
Fig. 3: Mirror Position Definitions

1.2 Concept of the Jet Mirror

The new concept mirror using jet flow control [4,5,6] is aimed at reducing the drag of conventional mirrors by using a passive flow jet control technique similar to those used for high lift slotted airfoils of aircraft [13].
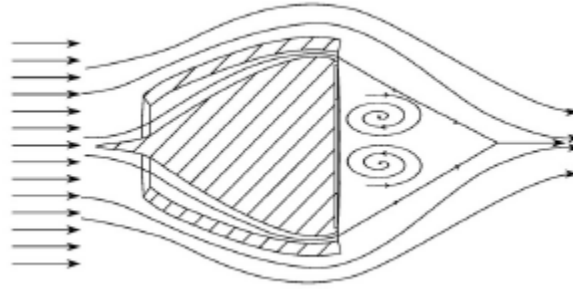
Fig. 4: Expected Flow Results

The above Fig. 4 is a basic, first concept, approximation of a jet mirror and the expected

flow structure. The flow inside the mirror is accelerated by the converging duct and by

the low base pressure at the exit. The main flow is at the highest velocity and lowest

pressure right before flow separation due to abrupt base geometry cut off. The CFD

results generally agree with that first concept, as can be seen below.   These results will

be further analyzed in the main body of the paper. See Fig. 5.
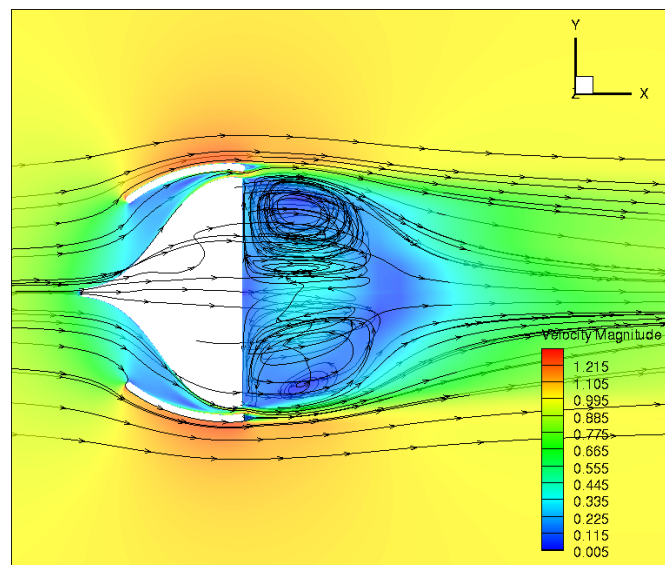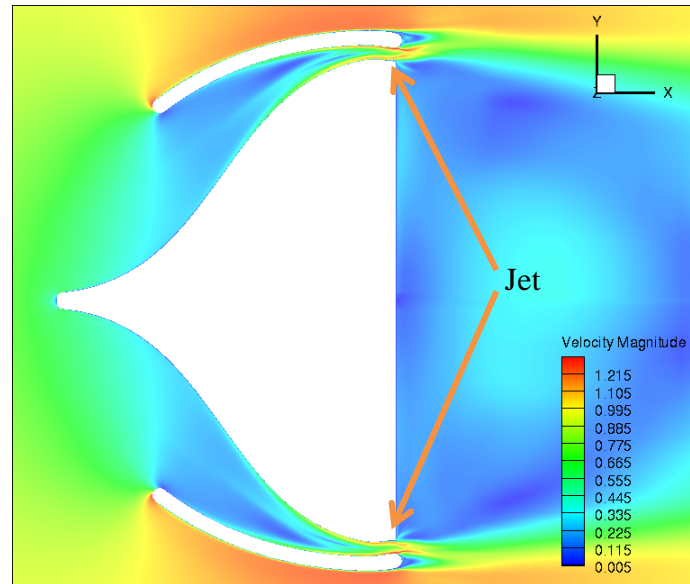
Fig. 5: Averaged Jet 2 Mirror Velocity Contours, Horizontal Mid-Plane

The aerodynamic jet mirror works for a few reasons [4,5,6]. Firstly, the jet harnesses high kinetic energy by capturing a large amount of free stream flow with a large inlet in the front. It renders the jet to exit the surrounding of the mirror in the low pressure zone and that jet brings high kinetic energy and high total pressure. These high energy jets create a mixing with the main flow thus creating large vortex structures, which entrain the main flow to the base flow thus energizing the base flow. Angling the jet toward the mirror center creates a more stable vortex zone behind the mirror. A more stable vortex mitigates the vortex shedding and turbulence fluctuation, which reduces wake size [11]. It is well known that the aerodynamic drag is directly determined by the wake width (Fig. 6).

$$D = \int_{\delta} \rho u (u_\infty - u) dy$$
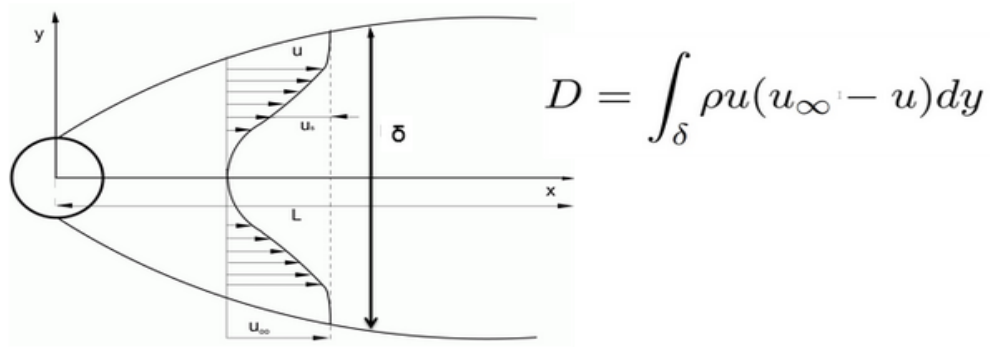
Fig. 6: Drag and Wake Relation

The above figure represents the drag force as a function of the difference between free stream velocity and the velocity in the wake region. The term u_∞ represents free stream velocity in the x-direction and u is the x-direction velocity at any point. The smaller the wake width, the smaller the drag. A shrunken wake size and energized base flow increases base static pressure. The opened inlet reduces the front blockage by passing the flow and decreasing the front area stagnation pressure area. All of these effects result in the reduced pressure drag.

The duct inside the mirror is designed to have no flow separation, the geometric parameters are important in determining the wake and vortex shedding mitigation including inlet area, area ratio of the inlet and outlet, and exit jet slot angle.

The larger the inlet area, the bigger the mass flow captured by the inlet, the higher momentum the exit jet will have. The area ratio of the inlet and outlet will determine the jet's exiting velocity. The higher the ratio, meaning a smaller jet exit area, the higher the jet velocity. The exit jet slot angle is to guide the jet direction as indicated in Fig. 4.

The jet momentum, velocity and jet direction are determined by these parameters and are expected to have a strong influence on the jet mixing pattern, even though the specific effects cannot be attributed to any certain parameter at this time.

By splitting the mirror into two parts, an inner shell component (center body with the mirror attached to it) and an outer shell (case) the concept of jet flow control can be applied. This method potentially reduces the drag compared to conventional mirrors by using flow control techniques similar to those used for slotted airfoils. The front of the mirror will have an opening inlet with a conical center body that introduces air flow, which is accelerated by a converging duct surrounding the center body. This airflow is ejected through a slot surrounding the mirror and located between the center body and the and the casing. The area of the inlet determines the capture area and the amount of air mass flow the inlet can introduce. The slot will produce a jet of air moving at a faster speed than the air that enters the inlet area and the air that moves around the outside of the casing. This jet should be angled to form a stable vortex zone behind the mirror. The jet 1 and jet 2 mirror designs can be seen below. The first set of pictures is jet 1 and the second set, jet 2. The picture in Fig. 7 is a translucent view of the jet 1 model from the top.

Outer Case
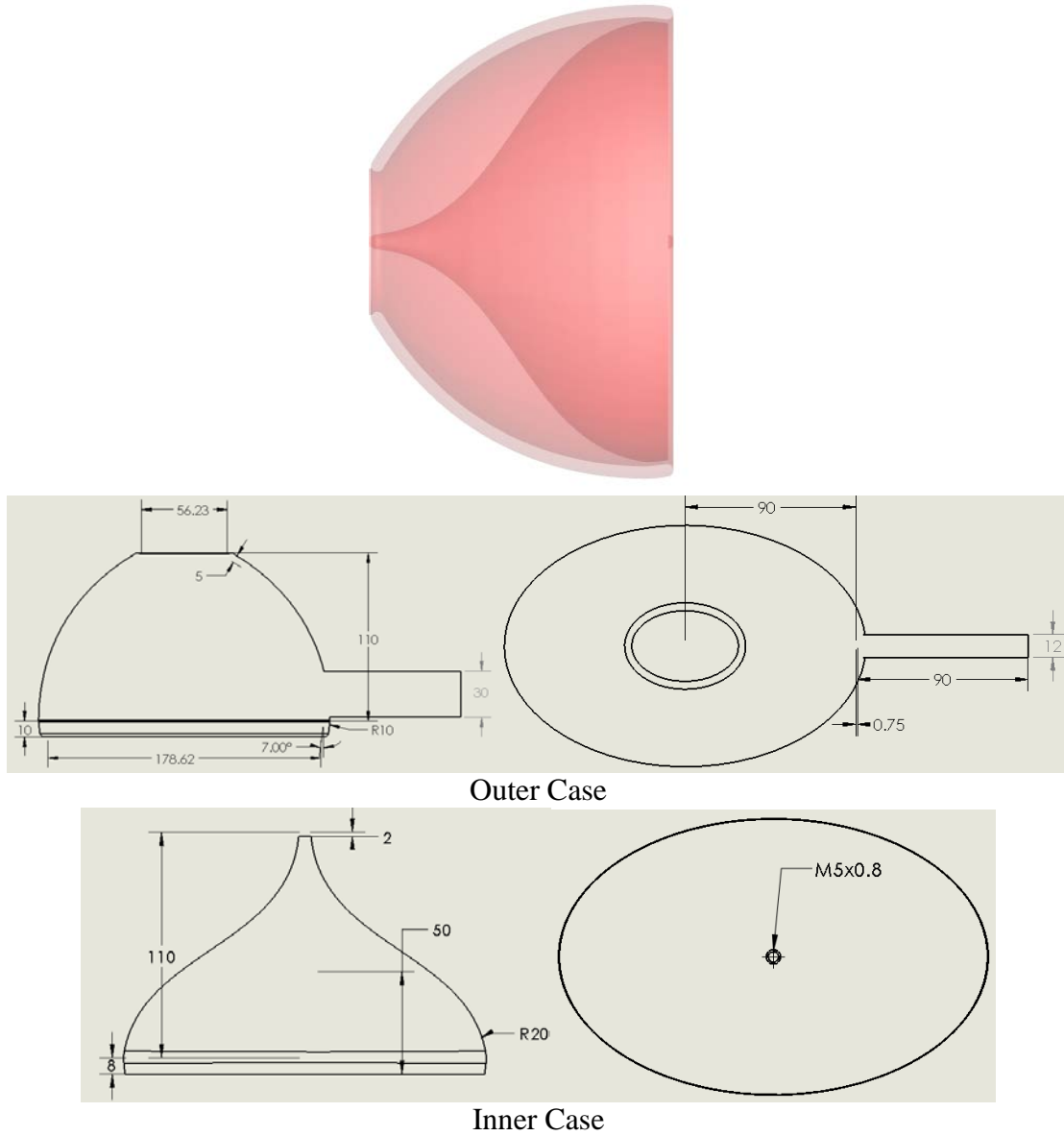
Inner Case

Fig. 7: Final Jet 1 Mirror Design

As stated earlier the jet 2 model (Fig. 8) has a larger inlet that further accelerates the interior flow.
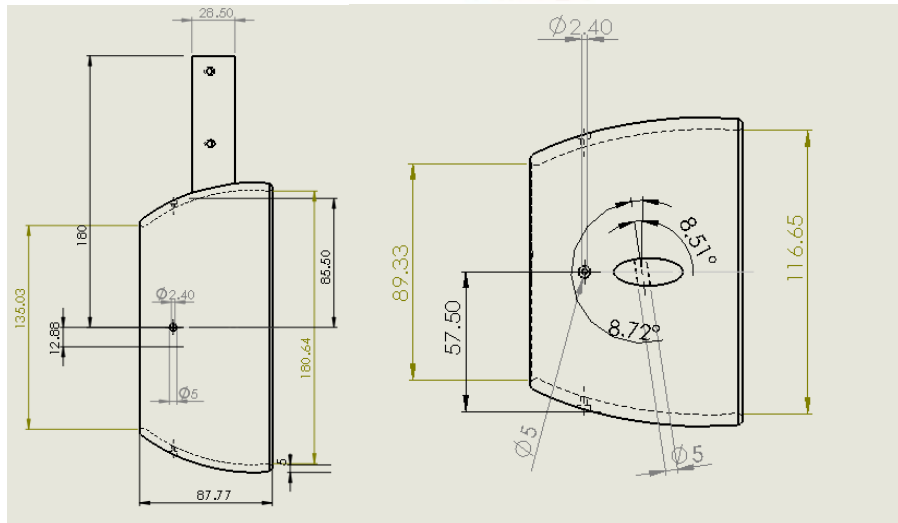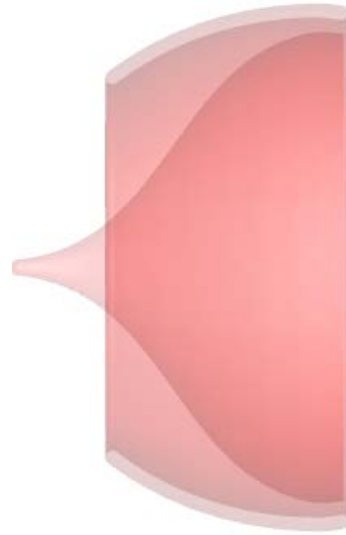
Outer Case
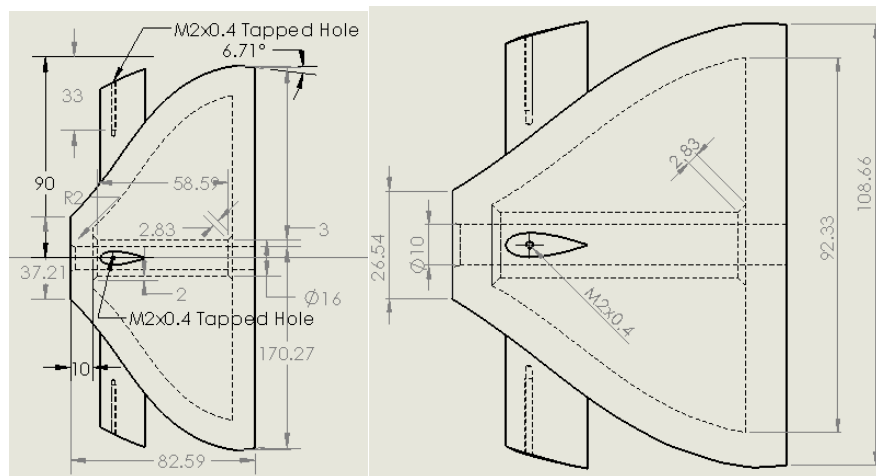
Inner Case

Fig. 8: Final Jet 2 Mirror Design

The jet mirror uses flow control techniques to reduce the drag that is created by current side-view mirror designs. This concept requires the creation of an entirely new scheme for side view mirrors since it features a shell system [20]. The U.S. NHTSA Standard 111 is upheld with this proposal as the functionality of the current side mirror is preserved. Since the design can emulate current side view mirror geometry, it would have low social impact as any visual differences are minimal. As long as this concept is thoroughly tested to evaluate its performance in reducing drag while ensuring it achieves stringent regulatory safety standards, it meets the initial design parameters and can be selected as a practical design.

The design maintains the general shape of current side view mirrors. The most common profiles for side view mirrors are smooth rectangular profile mirrors which are found on both cars and SUVs, flat square mirrors found on trucks and elliptical profile mirrors found on cars. The smooth rectangular and elliptical geometries do not feature sharp corners and are designed with aerodynamic considerations. Since side view mirrors differ among vehicle models, the proposed concept is based on a well-known car model with a side view mirror profile that can be easily emulated. The Mini Cooper is a popular car model that features an elliptical shaped mirror which loosely serves as the design basis. The simple shape provides an easy profile for making the SolidWorks model and a physical prototype. At the same time, the design is still viable to prove that the jet mirror concept works with an existing commercial mirror exterior. The actual Mini-Cooper

mirror has a cavity effect due to the recessed position of the mirror house relative to the

aft edge. Such a cavity effect is known to have some drag reduction effect and is not

taken into account in this study. In other words, the mirror face is in line with the edge of

the outer casing in both the baseline and jet models.

Fig. 9: Mini-Cooper Mirror

To develop a design for the first prototype, measurements of a Mini Cooper side view

mirror were taken. Fig. 9 shows a pair of these Mini Cooper mirrors. The back side of

the Mini mirror features an elliptical geometry with a smaller diameter of approximately

138 mm and a larger diameter of approximately 190 mm. The distance from the front of

the mirror to the back is approximately 127 mm as the casing becomes larger in the cross-

sectional area. The dimensions of this existing mirror are used to design our baseline

model, shown in Fig. 10.

Fig. 10: Final Baseline Mirror Design

It should be noted that all models are made out of an extremely smooth plastic material so that friction drag is as small as possible.

 Before the specifics of the jet mirror can be discussed, the larger purpose of the concept must be understood. According to Bernoulli's Principle (Eq. 2) when an incompressible fluid moves through varying sizes of a tube the fluid's speed changes [10]. As the speed of a fluid increases the pressure decreases; as fluid speed decreases pressure increases. For steady flow, the amount of fluid entering a tube must equal the amount leaving the tube. The converging duct acts as a tube decreasing in cross-sectional area from the front to the back of the mirror. In accordance with Bernoulli's Principle, this means that air entering the inlet area will be ejected at a faster speed than when it entered the inlet because of the converging duct feature.

$$\frac{1}{2}\rho V^2 + \rho g z + P = \text{constant} \qquad \text{(Eq. 2)}$$

 Under equilibrium, the total area of the inlet compared to the total area of the outlet will

determine the speed at which air traveling through the converging duct inside the mirror will be ejected. Bernoulli's Principle gives credence to the hypothesis that a larger inlet model will energize the base flow more than a smaller inlet model.

In summary, three prototype model configurations are studied in this paper: baseline, jet 1,and jet 2. From the inlet of the jet 2 design to the back edge, all outer casings are the same. The maximum section for the baseline model area is located at the back mirror surface and is an ellipse with an area of 18884 mm^2. This maximum surface area, which is perpendicular to the flow, is reduced by 3.6% and 9.7% respectively in the jet 1 and jet 2 designs. For both models the percent drag reduction is much higher than the percent area reduction, proving that the drag reduction is due to the jet design and not just the small change in area.

1.3 Objective

The objective of this thesis to demonstrate the advantages of the mirror design by large eddy simulation (LES) computational fluid dynamics (CFD) and wind tunnel testing and compare the CFD results with experiments. The in house high order accuracy CFD code (FASIP), is intensively validated in both 2D and 3D cases. In this case FASIP is used to model unsteady flows for LES analysis. Existing CFD code was used and slightly altered to make CFD plots for this project. This paper studies a baseline mirror design and two jet mirror designs with no optimization. The purpose is only to demonstrate the concept. Design optimization and refinement are problems that will be solved in future work.

Chapter 2

CFD Analysis of Baseline and Jet Mirrors

2.1 The Governing Equations

The Mach number and Reynolds number used in the numerical CFD simulation are .088

(roughly 30 m/s) and $2.60\text{x}10^5$ respectively. The proper Reynolds number was calculated

using the following formulation:

$$Re = \frac{u_\infty \rho L}{\mu}$$

(Eq. 3)

In this case the L used is the length of the baseline mirror from front to back.

The implicit LES methodology is used as applied by the in house CFD code, FASIP,

which stands for Fluid-Acoustics-Structural Interaction Package. The methodology of

the code has been proven to be accurate in past experiments [4,5,6,7,8,13,15,17,18,19].

The Roe scheme is used with the 1st order MUSCL scheme for the in viscid fluxes [15].

Second order differencing is used for the viscous terms. Contour results shown in this

paper are processed every 0.02 time steps.

Delving deeper into the fluid dynamics, the Navier Stokes equations must be broken

down. Navier Stokes Equations are the governing equations for all fluid flow problems.

Computational fluid dynamics uses iterative methods to solve these partial differential

equations. The generalized 3D Navier Stokes equation is shown in Eq. 4

$$\frac{\partial \mathbf{Q}}{\partial t} + \frac{\partial \mathbf{E}}{\partial x} + \frac{\partial \mathbf{F}}{\partial y} + \frac{\partial \mathbf{G}}{\partial z} = \frac{\partial \mathbf{R}}{\partial x} + \frac{\partial \mathbf{S}}{\partial y} + \frac{\partial \mathbf{T}}{\partial z}$$

(Eq. 4)

In the 3D Navier Stokes equation, **Q** represents the conservative variables and vectors **E**, **F**, **G**, are the flux vectors in the respective x,y and z directions. Finally **R**, **S**, **T** and are the viscous terms. Specifically:

$$\mathbf{Q} = (\rho, \rho u, \rho v, \rho w, \rho e)^T$$

$$\mathbf{E} = (\rho u, \rho u^2 + P, \rho uv, \rho uw, \rho(\rho e + p)u)^T$$

$$\mathbf{F} = (\rho v, \rho uv, \rho v^2 + P, \rho vw, \rho(\rho e + p)v)^T$$

$$\mathbf{G} = (\rho w, \rho uw\ , \rho vw, \rho w^2 + P, \rho(\rho e + p)w)^T$$

$$\mathbf{R} = (0, \tau_{xx}, \tau_{xy}, \tau_{xz}, Q_x)^T$$

$$\mathbf{S} = (0, \tau_{yx}, \tau_{yy}, \tau_{yz}, Q_y)^T$$

$$\mathbf{T} = (0, \tau_{zx}, \tau_{zy}, \tau_{zz}, Q_z)^T \qquad \text{(Eq. 5)}$$

In the above equations, ρ is density, u, v, w are the velocity components. The variable e is energy per unit mass. They are the basic variables calculated by the FASIP CFD software. From these five variables all aspects of fluid flow can be solved. A simple example would be a velocity magnitude equation:

$$V = \sqrt{u^2 + v^2 + w^2} \qquad \text{(Eq. 6)}$$

In Eq. 5 Q_x, Q_y and Q_z are the heat flux terms, which are functions of shear stress and velocity components.

To get the calculation started the user must give a few normalized initial conditions for the free stream flow. The following table gives the dimensionless input values which were used for both baseline and jet mirrors:

Variable	Value
Mach	0.088
P_{outlet}	92.23
P_{total}	92.73
Reynolds	260,000

Table 1: CFD Code Inputs

Where, P_{outlet} is the outlet static pressure of the free stream flow, P_{total} is the total pressure at the inlet of the free stream and the Mach number used is meant to reflect the free stream velocity of 30 m/s. All values were chosen in order to emulate the wind tunnel testing as closely as possible.

All of the equations in Eq. 5 can be solved simultaneously using various differencing schemes. Turbulence modeling of fluid flow is extremely complex and much research has gone into capturing this chaotic phenomenon. From this plethora of research many different approximation methods are attempted in order to give accurate results. Just to name a few, turbulence models include Detached Eddy Simulation (DES), Reynolds averaged Navier-Stokes (RANS), Direct Numerical Simulation (DNS) and Large Eddy Simulation (LES), . For this project, the LES model is used due to its ability to capture complex vortices. LES directly simulates the large eddy structures and the smallest sub-grid scale of the eddies, which is more isotropic and giving this model more plausibility.

The jet strength can be better quantified by a parameter such as the momentum

coefficient [16]:

$$C_\mu = \frac{\dot{m}V_{jet}}{1/2(\rho_o V_o^2 S)} \qquad \text{(Eq. 7)}$$

In the above equation $\dot{m}$ is the jet mass flow rate, ρ_o is the free stream flow density, V_{jet}

is the jet velocity, S is the jet area of the mirror and finally V_o^2 is the square of the

freestream velocity. The momentum coefficient results given in this paper are averaged

over 10 characteristic units of time. This parameter will be quantified and utilized in the

results section.

Lastly, Reynolds stress will be used to enumerate the turbulent zone behind the mirror.

Simply put the Reynolds stress is a part of the total fluid stress, which is gotten by

averaging the Navier-Stokes equations in order to account for turbulent changes in the

fluid's momentum. The formulation is as follows:

$$\tau_{R_{ij}} = -\rho \overline{u'_i}\,\overline{u'_j} \qquad \text{(Eq. 8)}$$

This is sometimes referred to as momentum flux. In this study the velocity x and y

velocity components will be used, (u, v).

2.2 Meshes

In solving any CFD problem, the first task is to generate a mesh within the flow field.

The FASIP CFD code that is used in the University of Miami CFD lab is no exception.

The mesh is basically an extremely intricate 3D grid, and for every point on that grid the

five basic conservative variables are solved for. The space of the mesh contains the geometry of a solid body that will interact with the flow. In the case of this project, the flow field contains either a baseline or jet mirror. In the mirror meshes, each cell is hexagonal in nature. This means for 2D meshing each cell has four node points at the corners and in this case the 3D mesh has eight node points per cell.

In the creation of any mesh there are two major factors that must be weighed against each other. Those two factors are the size of the mesh and the CPU time. The finer the mesh (more mesh points) the longer a CFD simulation takes. Due to the complex nature of the expected vortices, the mesh is much finer in the jet and base regions. In contrast the mesh is very coarse in regions distant from the mirror as we expect no flow separation or any flow of interest to this experiment in those regions. The mesh also accounts for the boundary layer fluid flow by transitioning from coarse to fine as a wall is approached. Since all three meshes are rather large, they are first split into smaller meshes called blocks and then submitted to the FASIP CFD code. By splitting the meshes it allows for an exponentially faster computing process utilizing an MPI (Message Passing Interface). An MPI is a parallel computing measure that processes all the blocks of a mesh at the same time rather than going through the blocks one at a time.

Structured hexagonal meshes are used for the baseline, jet 1 and jet 2 cases. The mesh sizes are roughly $6x10^6$ for the baseline case and $3x10^6$ for the jet cases. The baseline, jet 1, and jet 2 meshes contain 62, 40, and 50 blocks respectively. Baseline, jet 1, and jet 2 are displayed respectively in Fig. 11-13, which shows the mesh topology at the mirror's

cross section. For all three cases the far field boundary of the mesh is located at 20 times

the length of the mirror. Please note that no design optimization is done to any of these

models, which are only created only for the purpose of proof of concept. It is expected

that there is a large room to further improve the drag reduction by tweaking outlet flow

angle, mesh refinement around outer casing shape, and the duct inlet/outlet ratio.
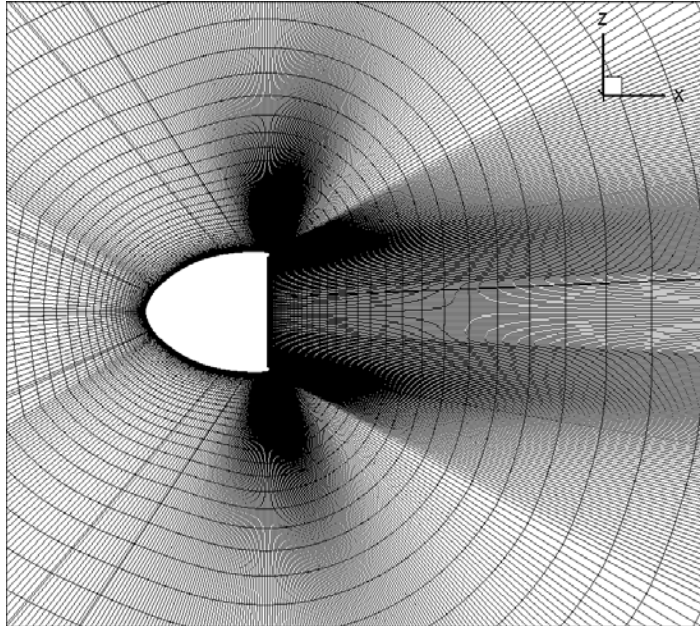
Fig. 11: Baseline Mesh
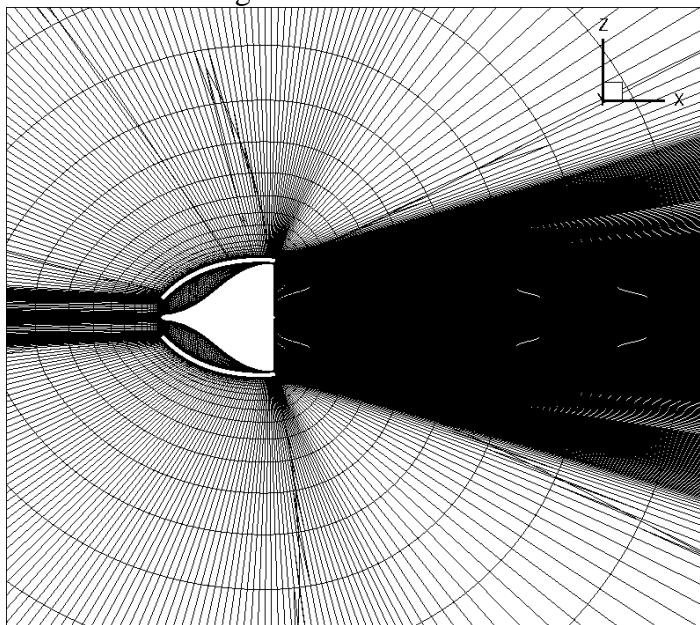
Fig. 12: Jet 1 Mesh
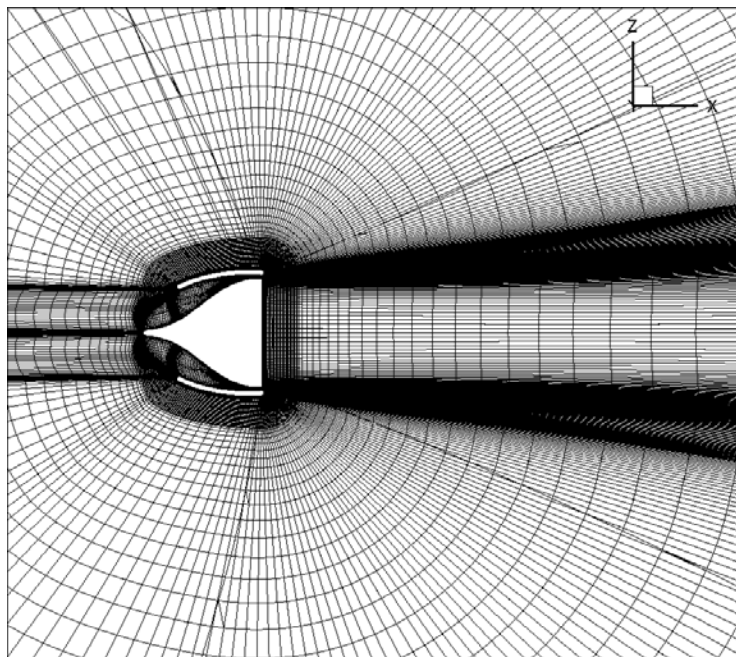
Fig. 13: Jet 2 Mesh

2.3 Result Discussion
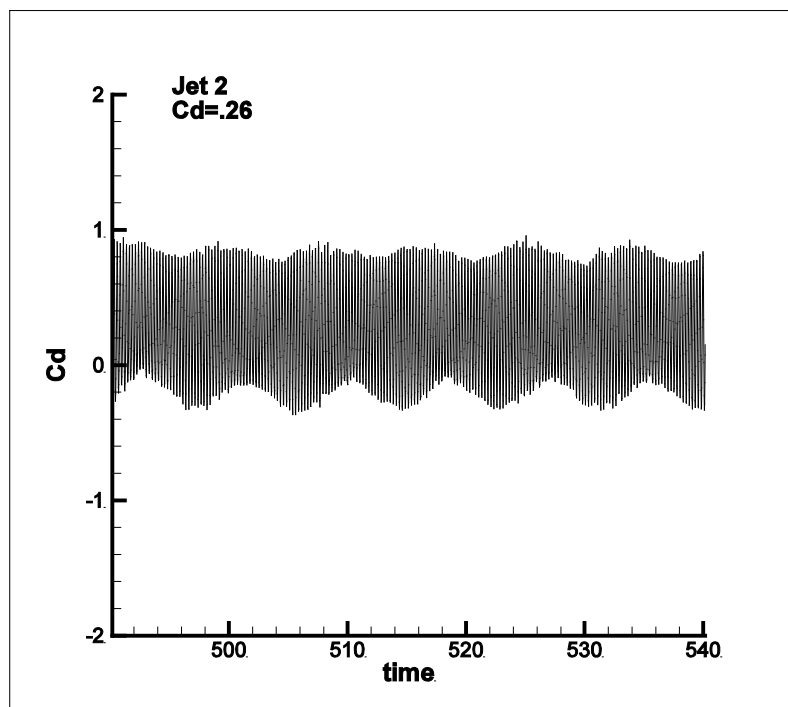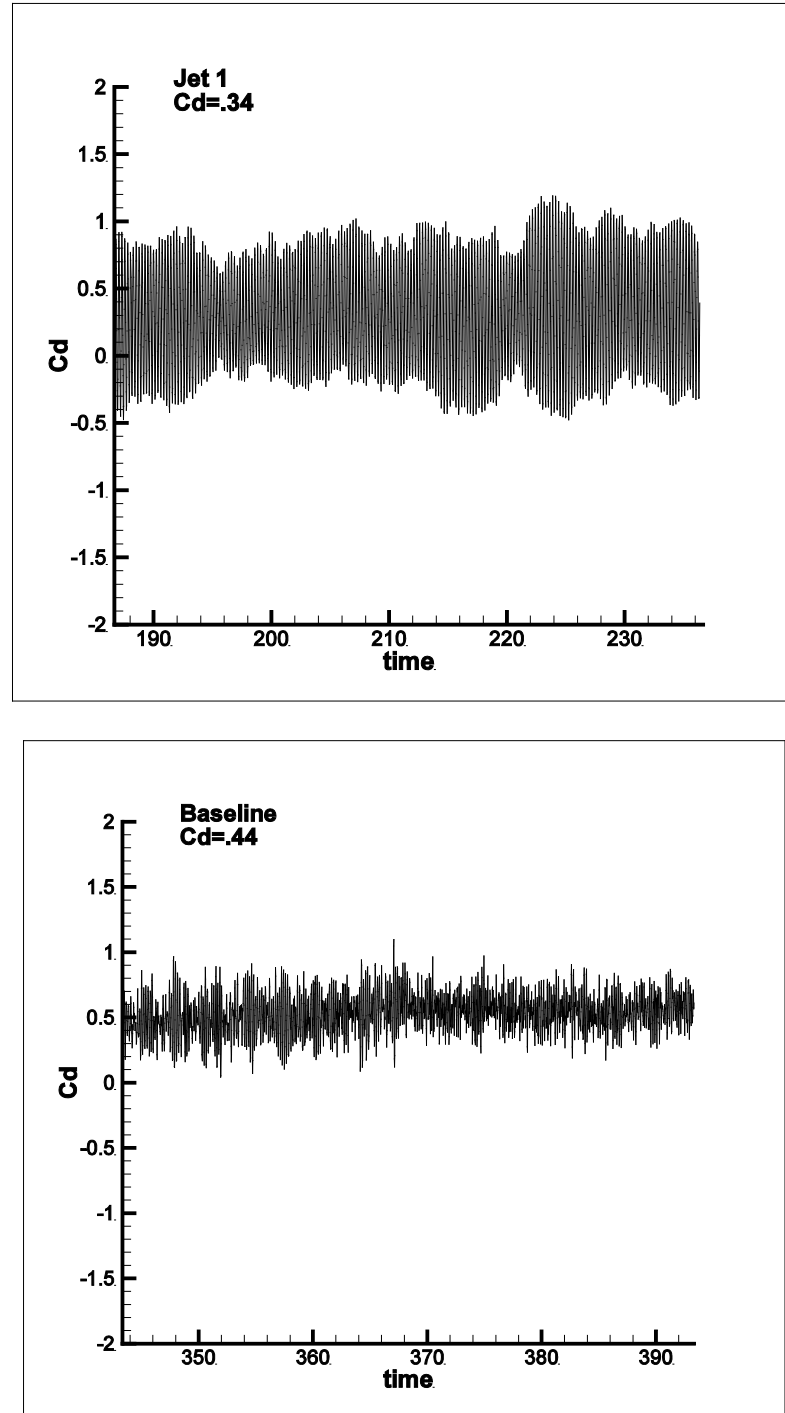
Fig. 14: Drag Coefficient History

Fig. 14 shows the time history of the computed drag coefficient of each design, which

indicates the drag fluctuation due to vortex shedding. The average drag coefficient is .26

for jet 2, .34 for jet 1 and .44 for the baseline model.   Vortex shedding is an oscillating

flow that happens when a fluid flows past a bluff body. In this type of flow, vortices are

created at the back of the mirror. These vortices continuously detach from the mirror

body creating a fluctuation in drag.

	Cd	Strouhal	Drag Reduction
Jet 2	0.26	3.97	40.91%
Jet 1	0.34	4.1	29.41%
Baseline	0.44	3.204	

Table 2: CFD Drag Coefficient Results

Table 2 summarizes the computed drag coefficients of the different models. The data

shows that increasing the inlet size from the jet 1 to the jet 2 model greatly decreases the

drag. Table 2 also lists the Strouhal number of each case, which is a dimensionless

number that describes oscillating flow mechanisms.

$$St = \frac{fL}{V}$$

(Eq. 9)

In this case the Strouhal number is the rate at which the vortex is fluctuating and it can be

seen the Strouhal number is about 26% higher in the jet cases.

In order to visualize these fluctuations the downstream x-component velocity is plotted. .

The velocity contours with streamlines of the jet 2 model is shown below at two different

moments in time:
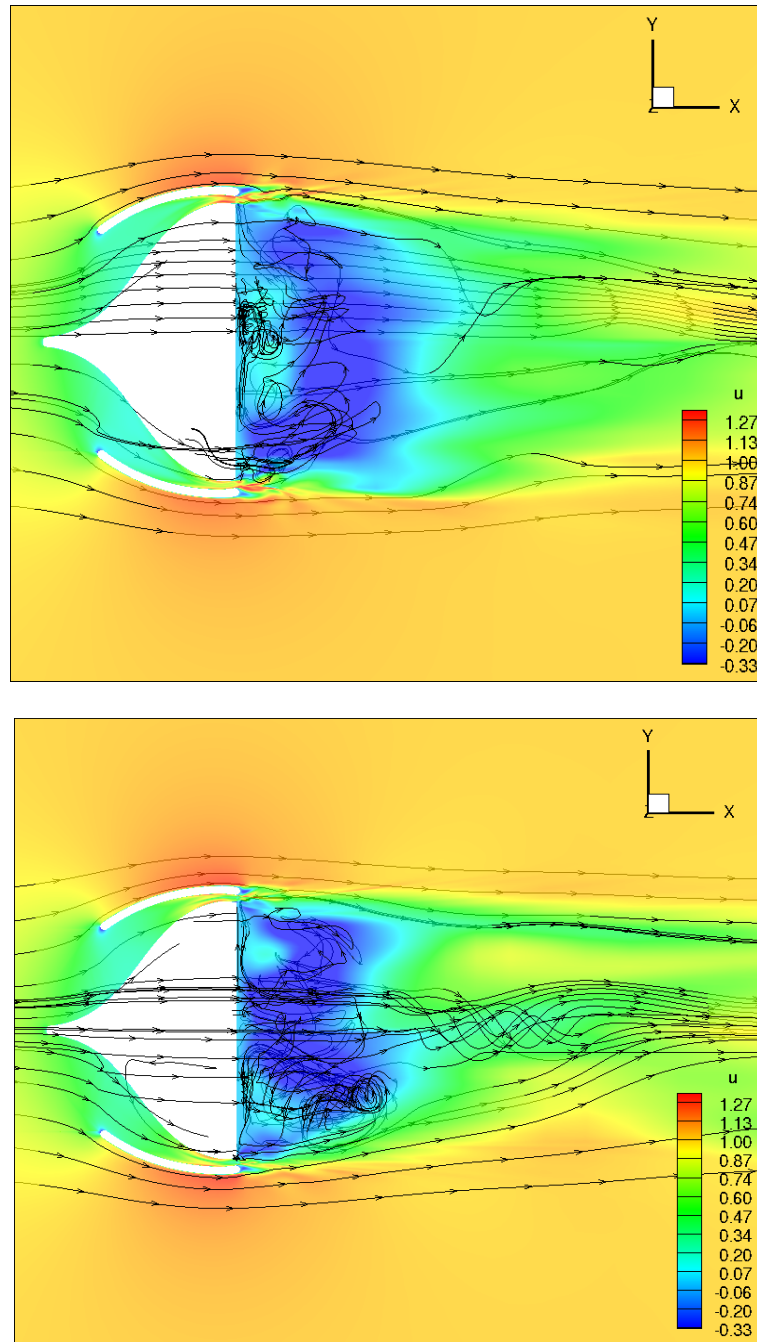
Fig. 15: Instantaneous Velocity Component Contours

Clearly the flow is highly unsteady and varying rapidly, but how? In order to answer that

question a movie is made by stringing hundreds of instantaneous plots together. A

surprising but clear observation can be made from these movies; the jet is pulsing. At

one moment in time the jet is strongly projecting from the outlet, at another moment the jet is in a formative stage. Movies are made for both cross-sections and stills of those movies are shown below to demonstrate the pulsing. Each instantaneous plot is generated by the Tecplot software and then strung together in movie form by another software called Virtual Dub.
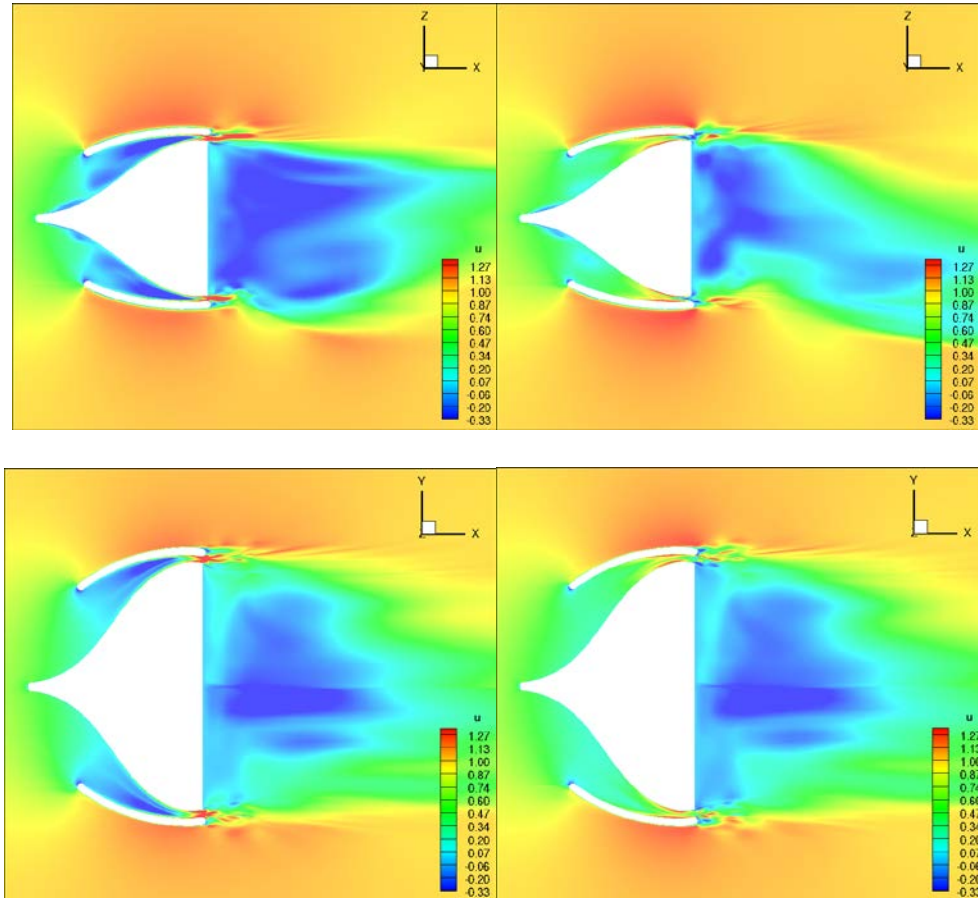
Fig. 16: Velocity Contours Showing Pulsing Jet
(top: vertical mid-plane; bottom: horizontal mid-plane)

The real surprise comes when the two different slices are compared at the same instant in time. The strength of the jet on the vertical mid-plane and the horizontal mid-plane has a 90 degree harmonic phase shift. That is when the jet on the horizontal plane is weak, and vice versa, as shown in Fig. 17.
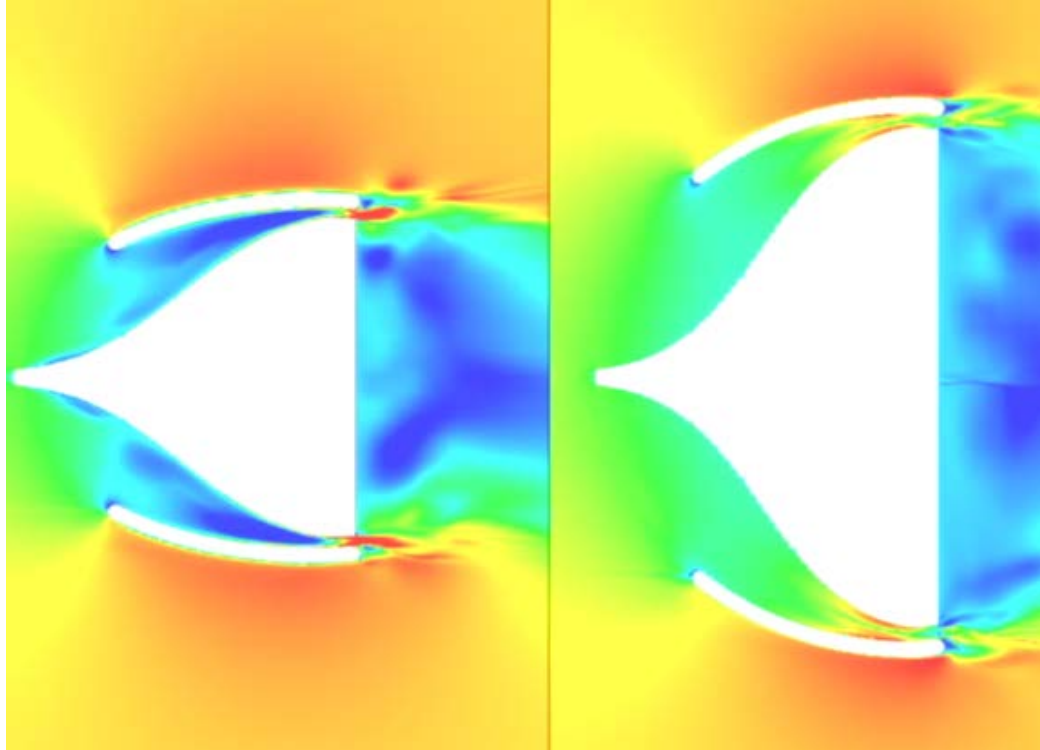
Fig. 17: Comparison of Velocity Contours Showing Phase Difference

This phenomena should be further investigated to see if the Strouhal number and jet frequency have any correlation.

Dozens of contour plots are made to better understand the fluid physics and better explain drag reduction. Fig. 18 shows the instantaneous velocity magnitude at the semi-minor axis plane section. The wake size and intensity of the jet models is significantly reduced compared with the baseline mirror.
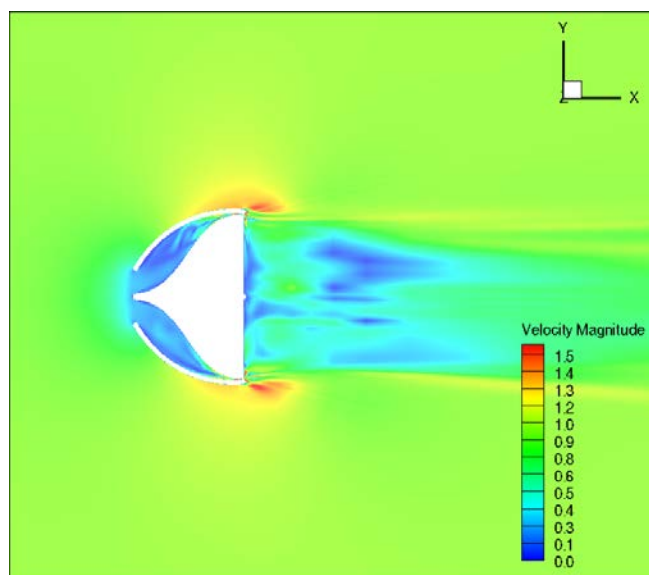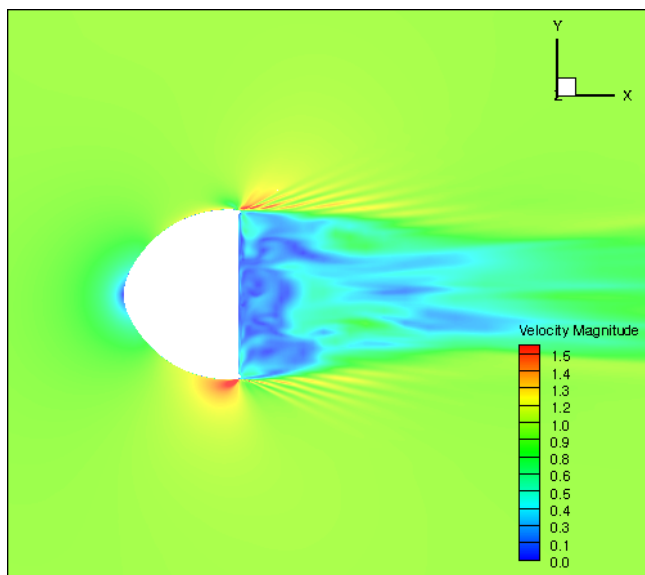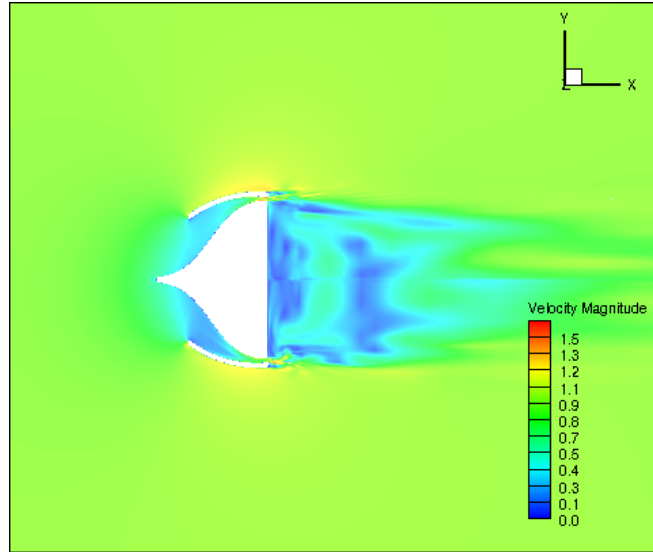
Fig. 18: Instantaneous Velocity Contours

Fig. 19-21 is the zoomed average x-component velocity magnitude contours at the
maximum horizontal cross section, but this time zoomed in on the jet region. The
baseline mirror flow reaches the maximum speed at the base edge and a low pressure
base flow is formed at the base due to the base flow.
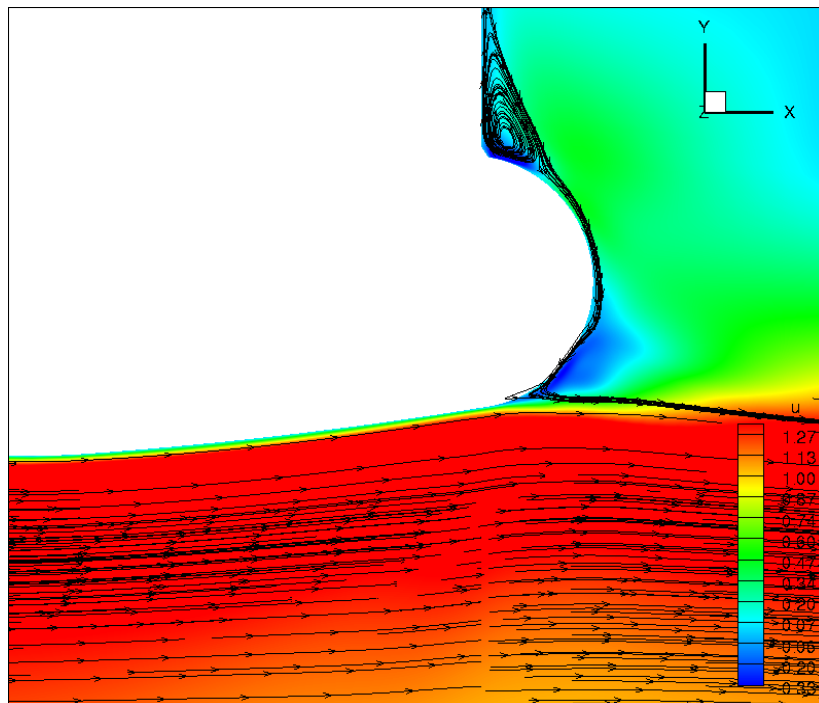
Fig. 19: Average Zoomed Baseline X-Component Velocity Contours
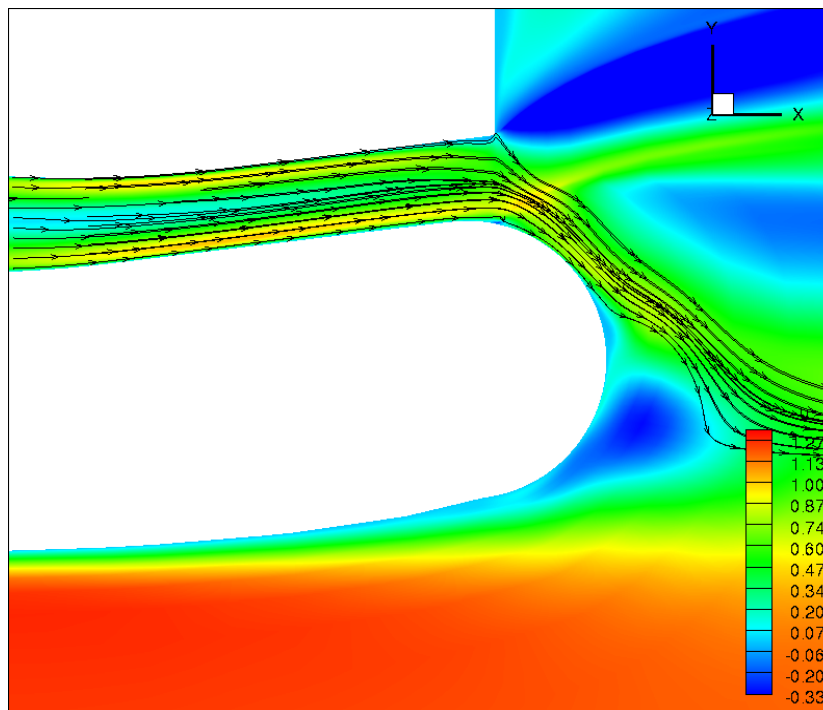
Fig. 20: Average Zoomed Jet 1 X-Component Velocity Contours
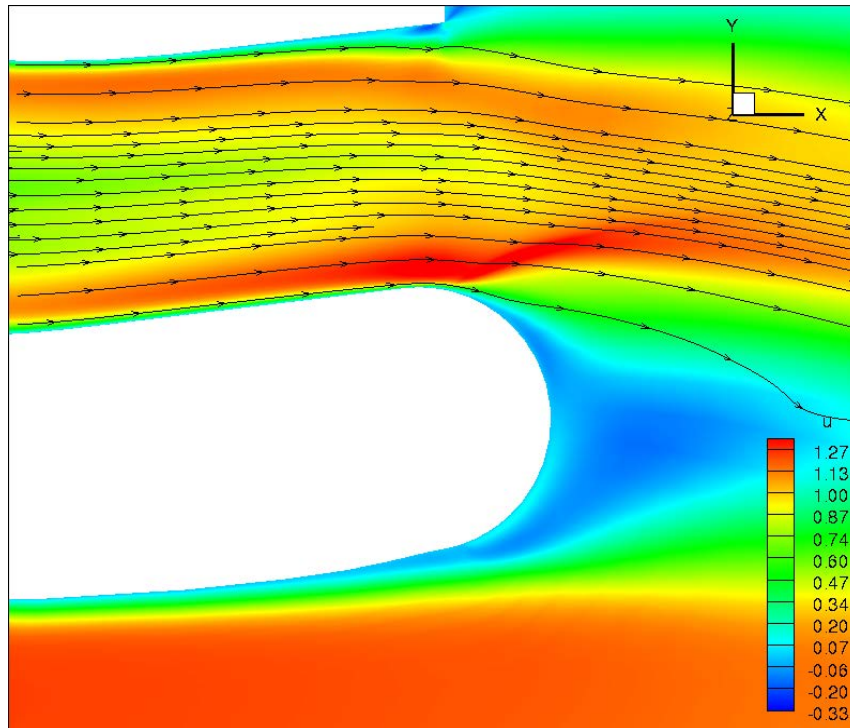
Fig. 21: Average Zoomed Jet 2 X-Component Velocity Contours

Fig. 20 shows that the jet is being sucked into the free stream flow rather than the base flow. This is due to the high total pressure of the energized jet, which gives a higher static pressure than the main flow. Hopefully this phenomena can be counteracted in future designs. Based on the time averaged u velocity contours, the velocity difference between the jet and the ambient flow outside of the mirror wall at the same x-location as the jet is important. Specifically, what is of interest is how different the jet is from the flow right outside of the jet. That velocity difference determines the vortex structure. In the jet 1 model the jet is 64% of the ambient flow and the jet 2 model jet comes in a little higher at 76%.
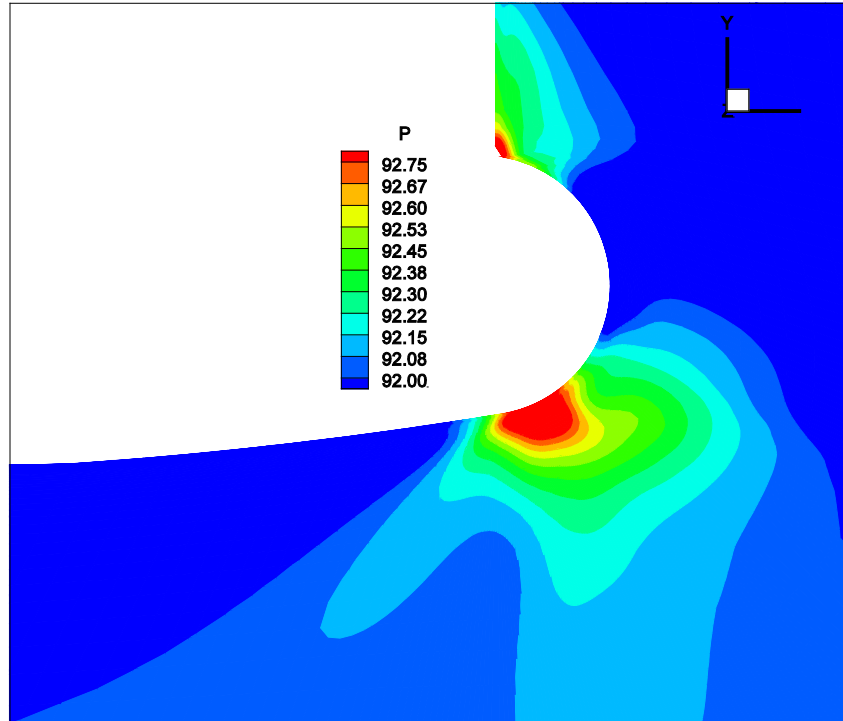
Fig. 22: Average Zoomed Baseline Pressure Contours
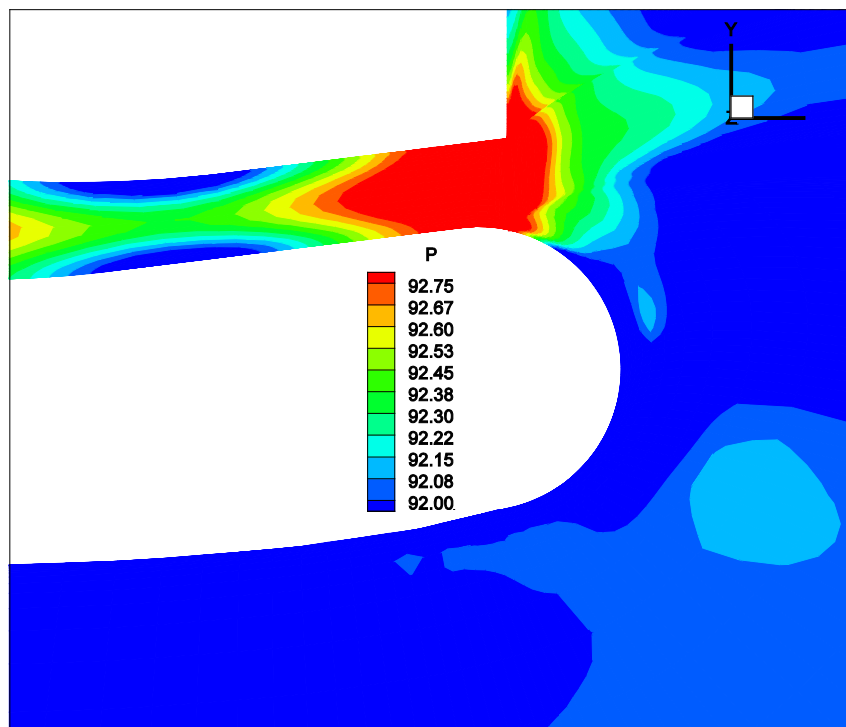
Fig. 23: Average Zoomed Jet 1 Pressure Contours
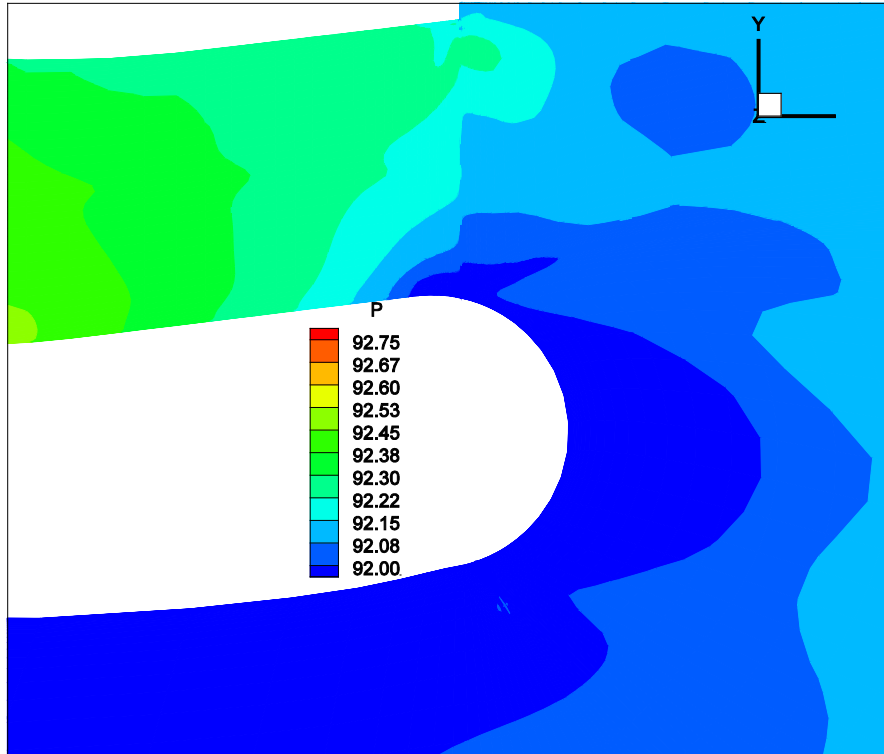
Fig. 24: Average Zoomed Jet 2 Pressure Contours

Fig. 25 is the x-component velocity contours over 10 characteristic time.
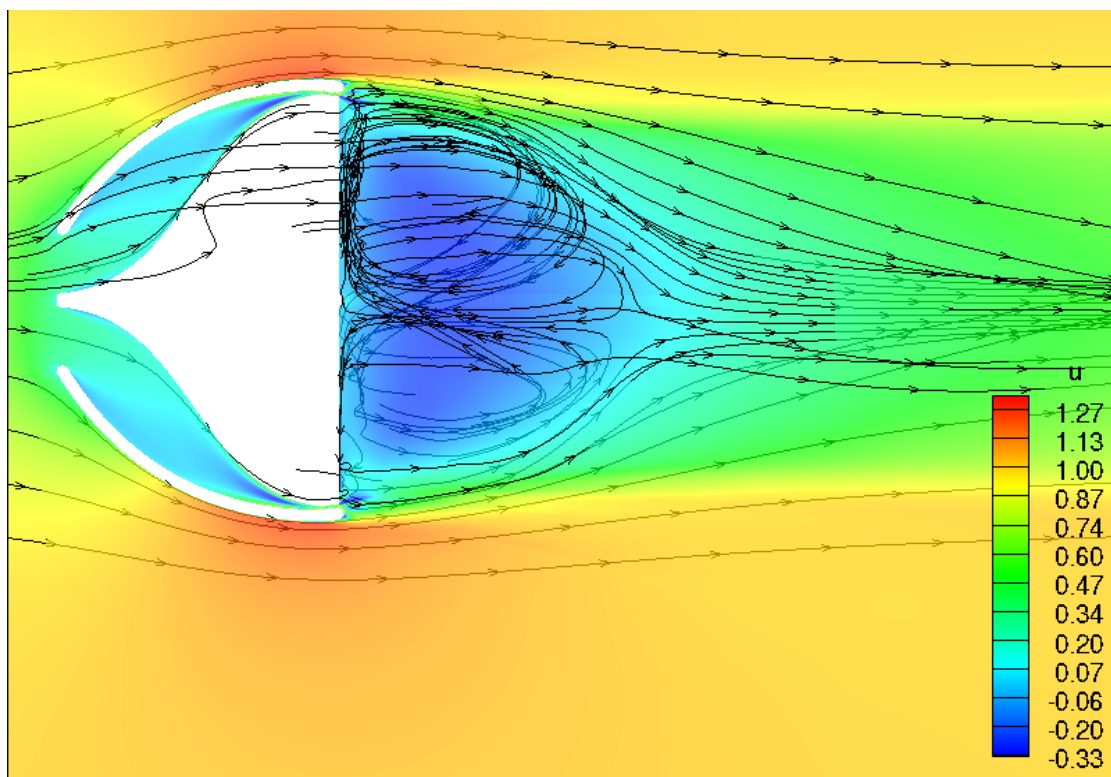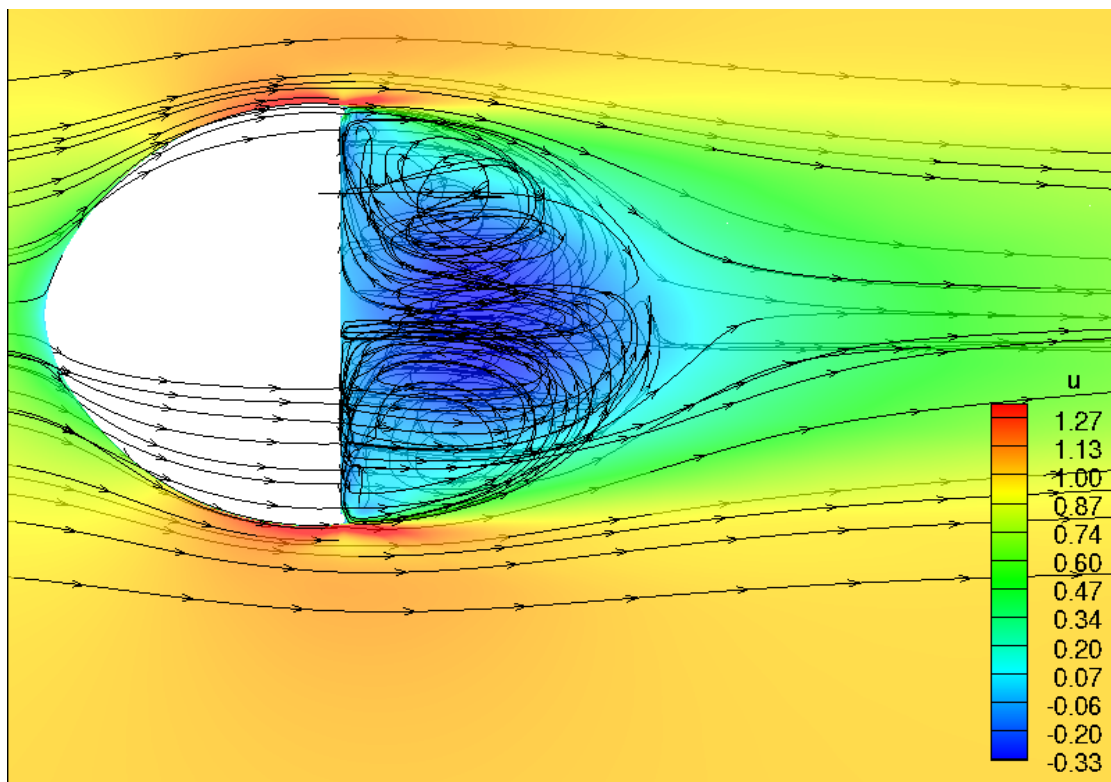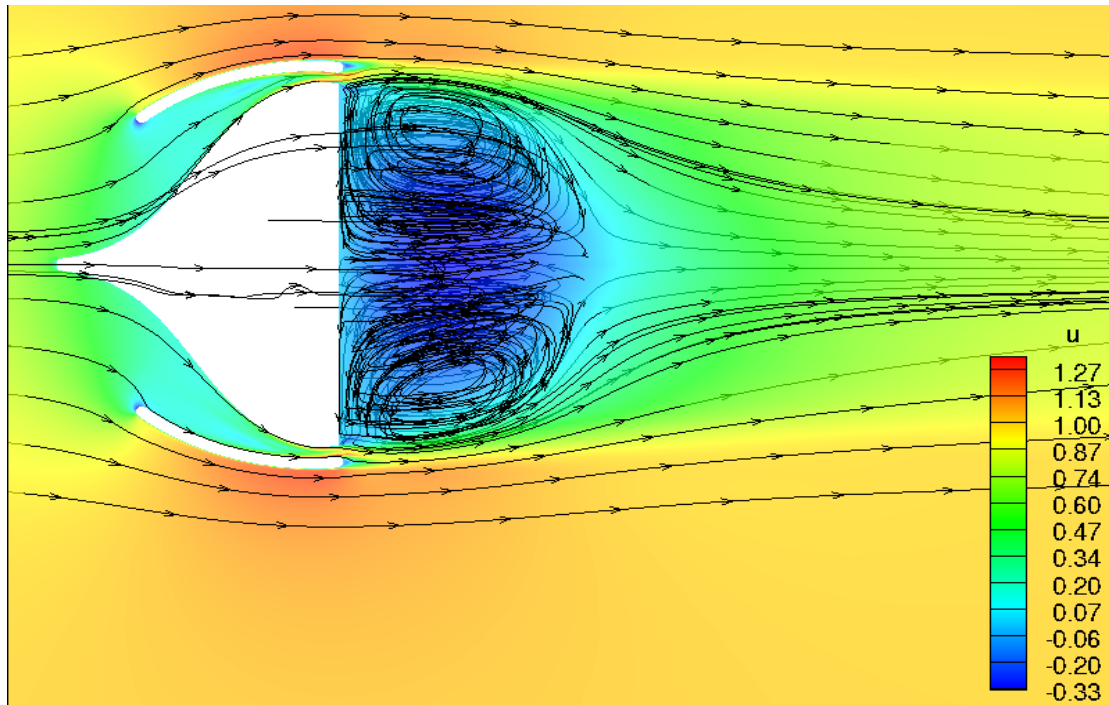
Fig. 25: Averaged Velocity Component Contours

Similar to the instantaneous plots, for the jet models, the flow reaches the maximum speed at the jet exit and is sucked outward to merge with the main flow again because the jet has higher static pressure and total pressure. While the jet 2 design has a noticeably shorter recirculation zone, it is obvious the wake width is been reduced. In order to better quantify this, measurements of u, the x-component velocity, are taken at a mid-span plane, 1.5 mirror lengths downstream. That measurement is plotted in Fig. 26 where u is averaged over 100t:
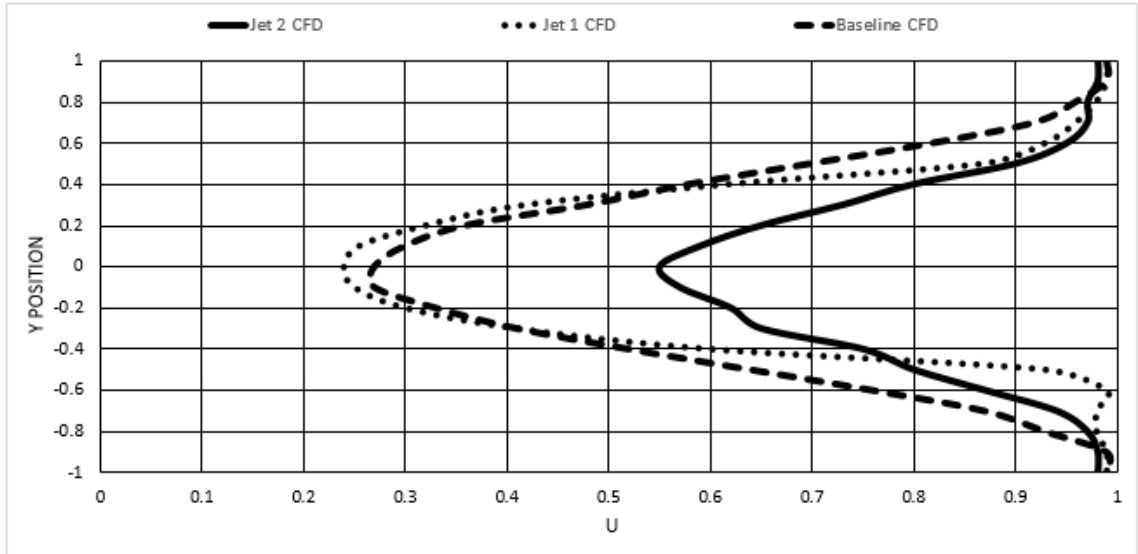
Fig. 26: Downstream Velocity Component Plot (CFD)

The u measurement in Fig. 26 is normalized by the free stream velocity. In all cases, near the top and bottom of the mirror the flow almost reaches free stream. As expected the jet 2 wake is both thinner and shallower. On the other hand the jet 1 wake presents less significant wake reduction. The wake seems to be thinner wake but also slightly longer.

To further understand and solidify the wake reduction properties of the jet mirrors, the above wake results in Fig. 22 are quantified into a singular number. By measuring the area between the curve and the vertical line at $u = 1$, one can exactly surmise the "wake area". This wake area is obtained using a Mathematica script, the results of which are shown here:

	Wake Area	% Reduction
Jet 2	0.378	45%
Jet 1	0.6	13%
Baseline	0.691	

Table 3: Wake Area Results

Now, with certainty, wake reduction is proven. The exact Mathematica script can be seen in Appendix III.

In order to visualize the energy loss, Fig. 27 displays the entropy contours at the constant axial location one and a half mirror lengths downstream of the mirror surface accompanied with a horizontal slice view. It can be seen that the baseline mirror has a much larger downstream high entropy area than the other two jet mirrors. The jet 1 mirror significantly reduces the downstream entropy footprint as compared to the baseline mirror, with the jet 2 mirror we see the entropy reduction is even greater.
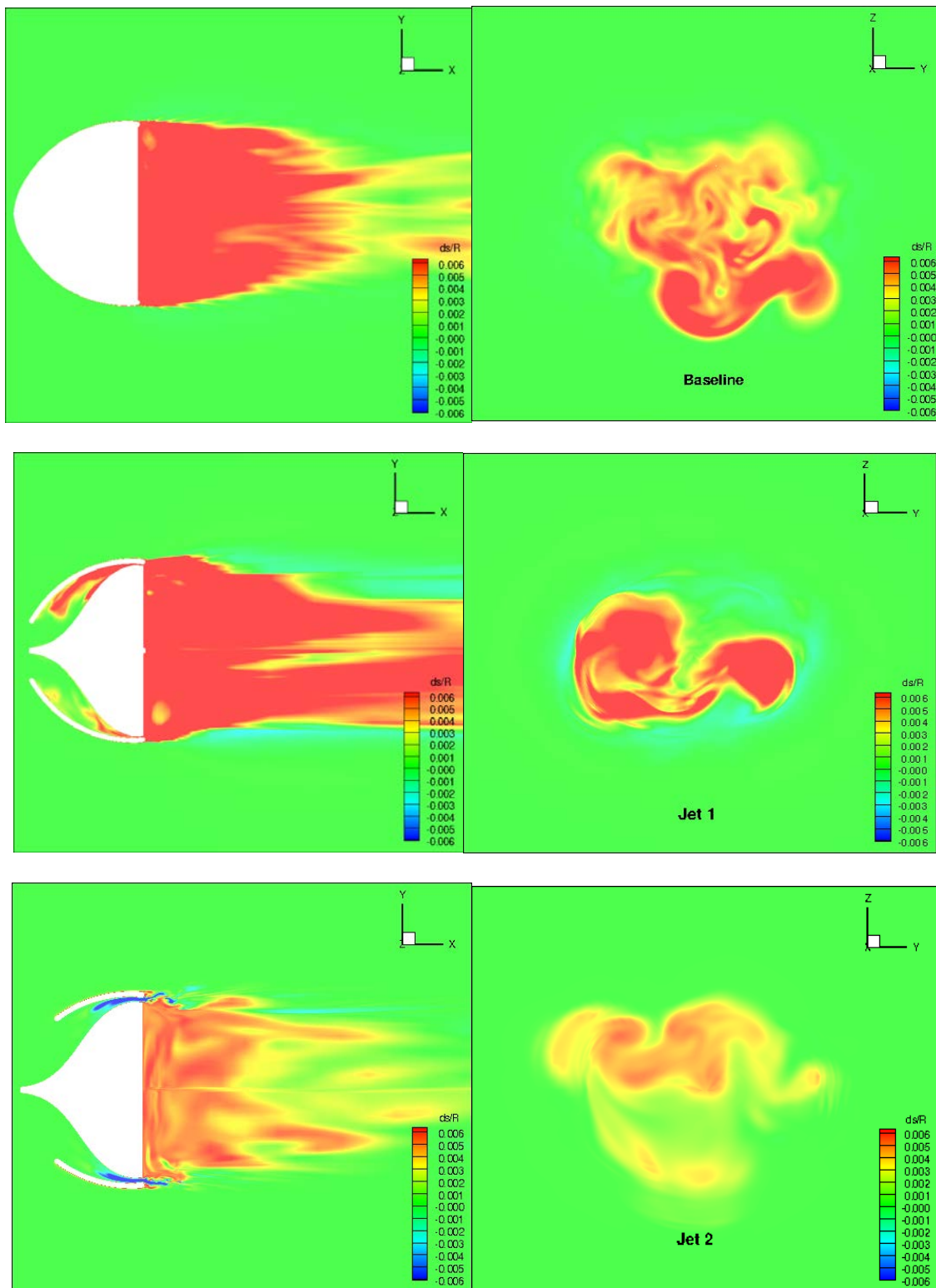
Fig. 27: Instantaneous Entropy Contours

The averaged cross-sectional entropy is also of interest in order to see how the jet

energizes the base flow over a period of time. The following are time averaged entropy

contours (Fig. 28) averaged over 100 units of time.
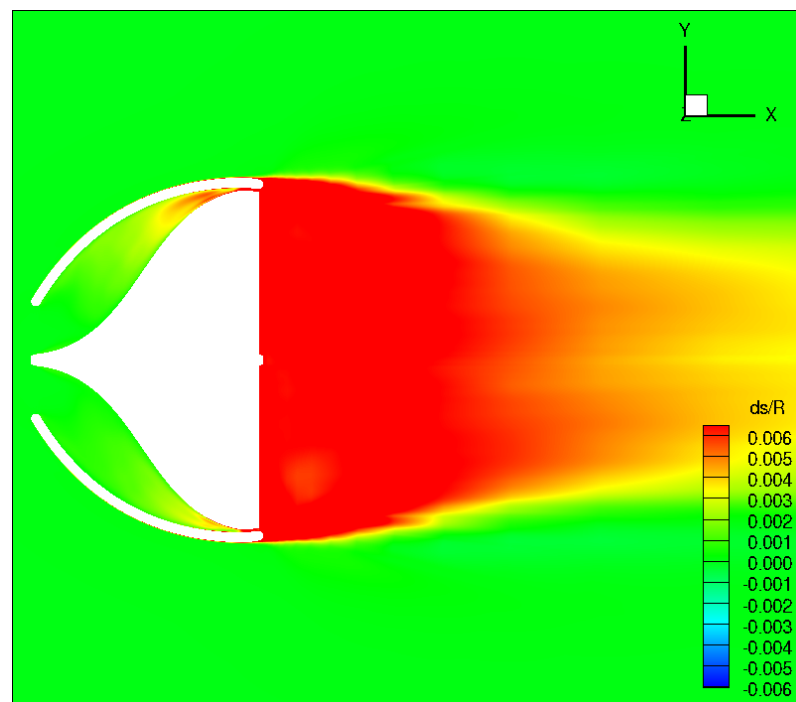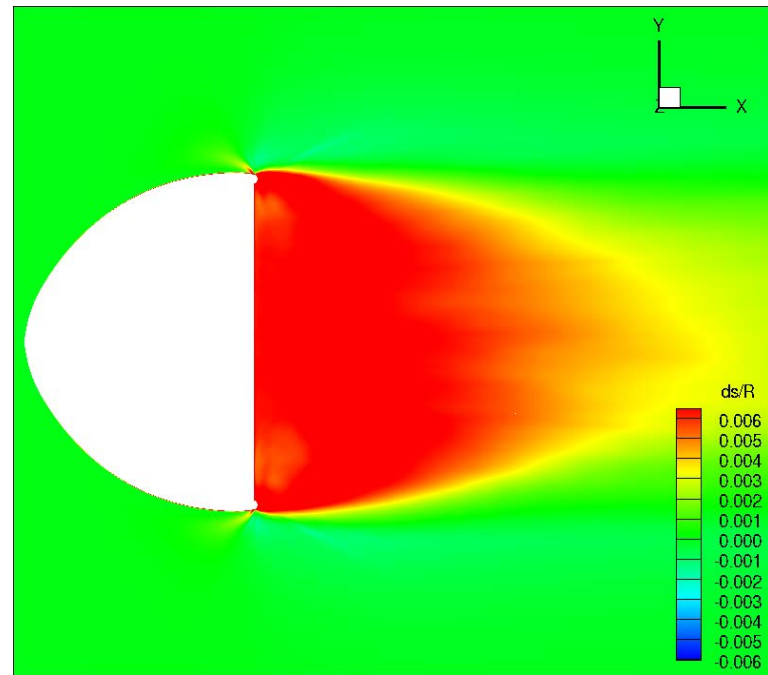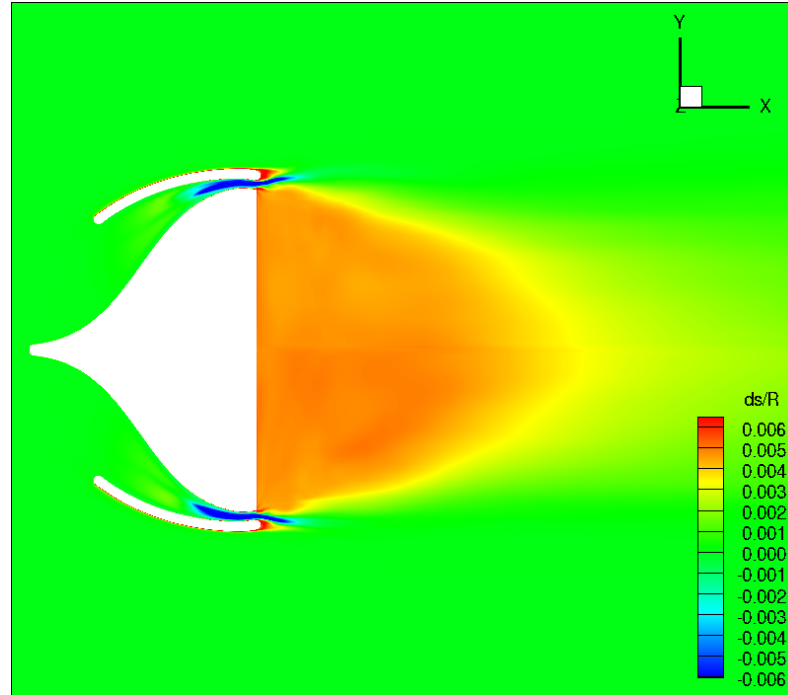
Fig. 28: Time Averaged Entropy Contours

Shockingly, the jet 2 model seems to be actively adding energy to the jet with negative

entropy. How is this possible? If Crocco's theorem is applied, one can more easily see

how this is physically conceivable.

$$T\nabla S = \frac{\partial V}{\partial t} + \nabla(H_0) - V \times (\nabla \times V) \qquad \text{(Eq. 10)}$$

Depending on the total enthalpy gradient, partial derivative of velocity the vector and

vorticity transportation, entropy can indeed by negative. This local effect may be caused

by high unsteadiness, acoustic waves or the vortices themselves.

Ultimately, for drag reduction, what is of the most interest is the surface pressure on the

mirror to examine if the pressure drag is reduced. Fig. 25 shows that the baseline mirror

has a large high pressure area in the front due to the stagnation region. Also, on the

baseline mirror base area, the pressure is lower and fairly uniform. The jet 2 mirror, shown in Fig. 26, shows the base mirror surface has an area of high pressure (orange color), which will contribute to pressure drag reduction and a smaller wake. The jet exit is also be seen with high static pressure due the jet being energized.
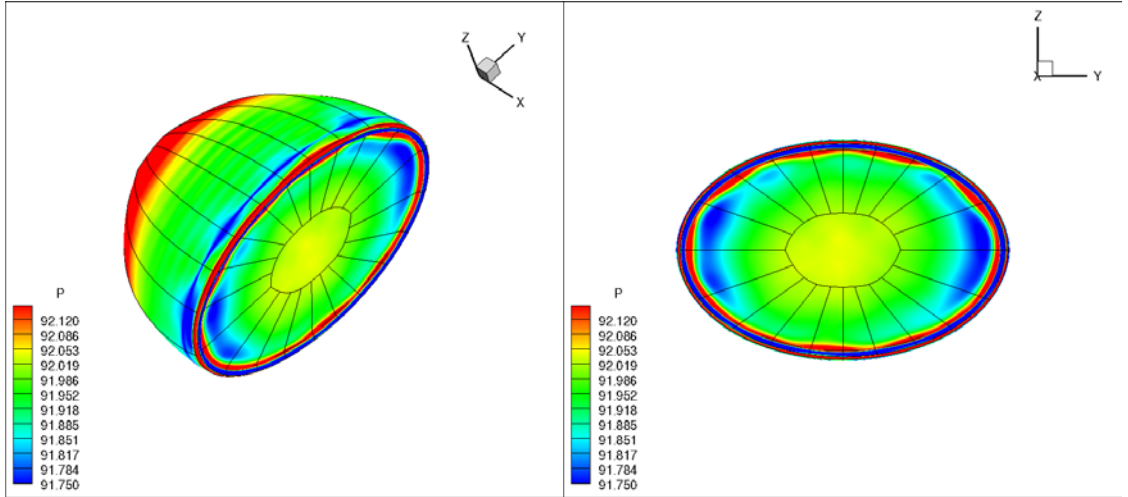
Fig. 29: Averaged Baseline Surface Pressure Contours
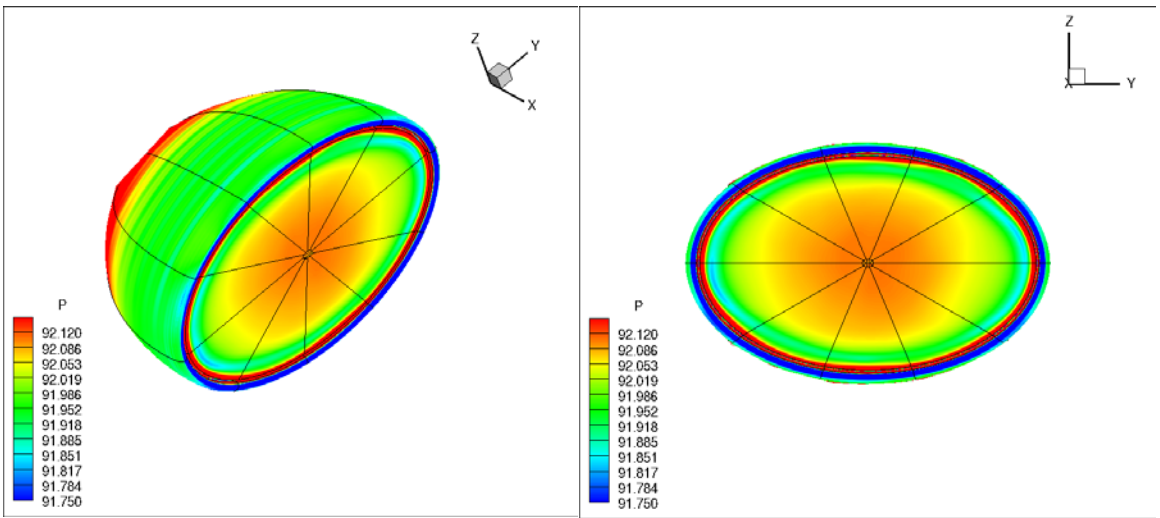
Fig. 30: Averaged Jet 1 Surface Pressure Contours
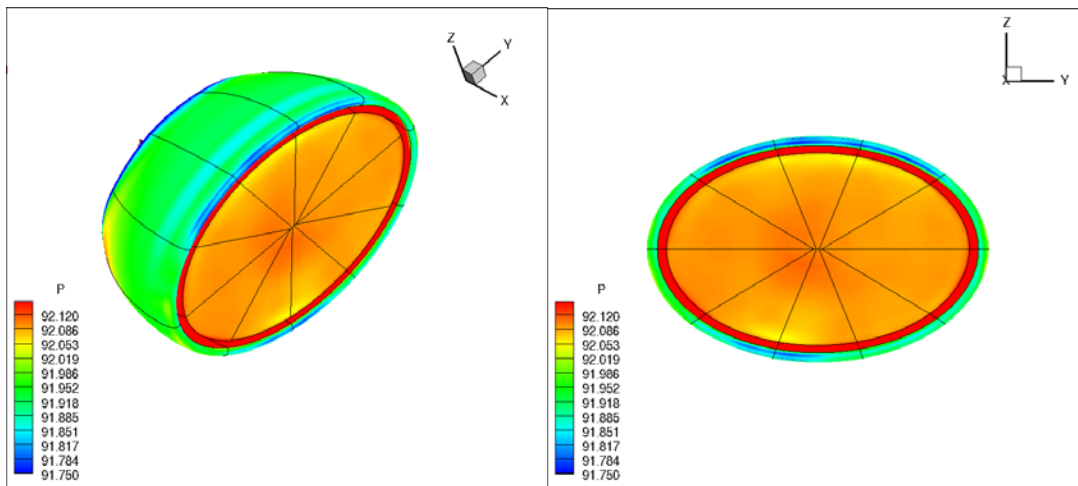
Fig. 31: Averaged Jet 2 Surface Pressure Contours

Not only can the surface pressure of the jet be found but one can also investigate the

coefficient of momentum at the jet.

Dimensionless	C_μ	Velocity	Mass Flow
Jet 2	0.078	0.622	0.073
Jet 1	0.039	0.610	0.039

Table 4: Dimensionless Momentum Coefficient Results

Dimensional	C_μ	Velocity (m/s)	Mass Flow (kg/s)
Jet 2	0.078	18.7	0.0053
Jet 1	0.039	18.3	0.0013

Table 5: Dimensional Momentum Coefficient Results

Table 4 shows that both the jet 1 and jet 2 models have jets that are about 60% of the free stream speed with the jet 2 velocity being slightly higher. Results also show that the jet 2 mirror momentum coefficient is double that of jet 1. This suggests that the mass flow and velocity of the jet, averaged over time, is greater in the jet 2 model. Due to the larger inlet and outlet these results make sense. When specifically processing the mass flow and velocity, one can see that the jet velocity is about the same but the mass flow in the jet 2 case is nearly double that of the jet 1 model. A larger and more powerful energized jet should indeed have a greater mass flow. Specifically, the variables used in Table 5 calculations are: $S_1 = .001132 \text{ m}^2$, $S_2 = .002265 \text{ m}^2$, $V_\infty = 30 \text{ m/s}$, $\rho_\infty = 1.27 \text{ kg/m}^2$.

The Reynolds stress is computed at .15 mirror lengths downstream at the mirror's centerline. One notices that the Reynolds stress seems to have the highest magnitude in the area between the centerline and the mirror centerline. Also, the jet 1model has noticeably higher magnitudes.
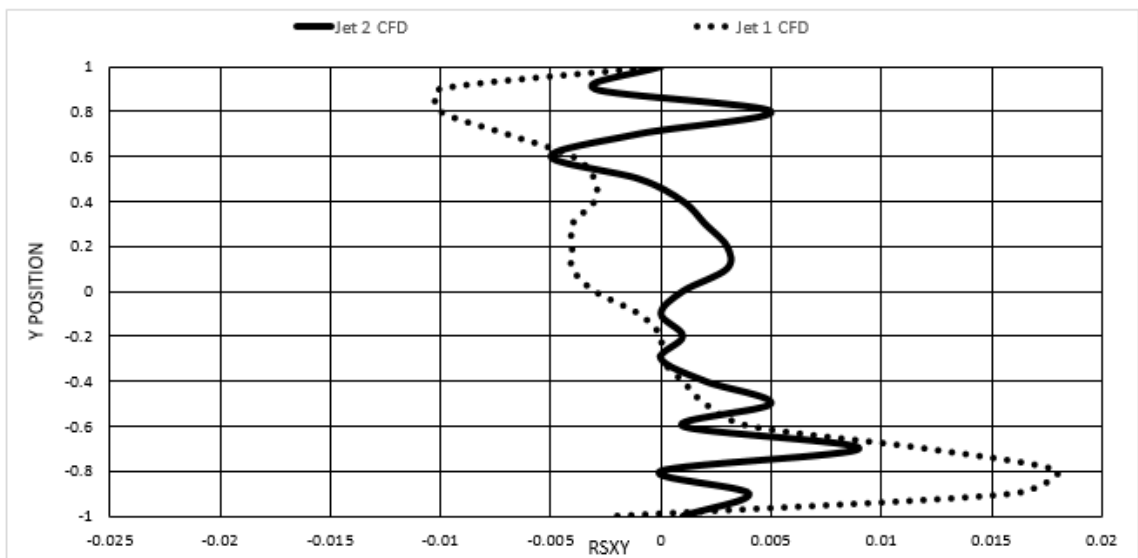
Fig. 32: Reynolds Stress Results

2.4 High Reynolds Conditions

Simulations are also run with a higher Reynolds number of 2,600,000 to investigate the

passive jet flow effect at a high Reynolds number. For example, the passive jet flow

control concept could be applied to road vehicles such as commercial trucks, which have

a high Reynolds number. Drag and Strouhal measurements are taken for the higher

Reynolds condition:

High Reynolds	Cd	Strouhal	Drag Reduction
Jet 2	0.22	6.24	64.52%
Jet 1	0.27	6.25	56.45%
Baseline	0.62	4.61	

Table 6: High Reynolds CFD Drag Coefficient Results
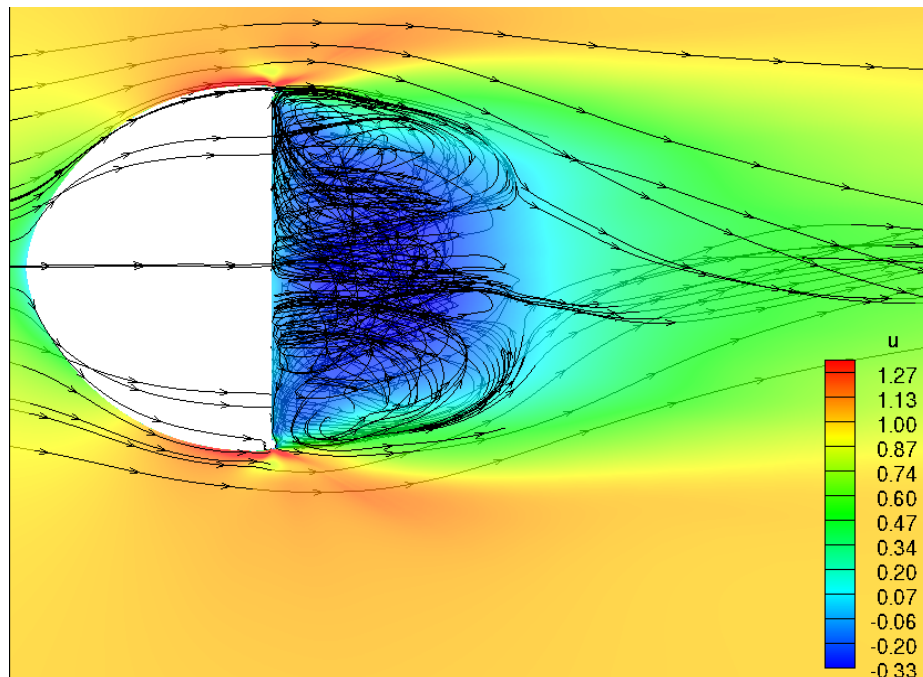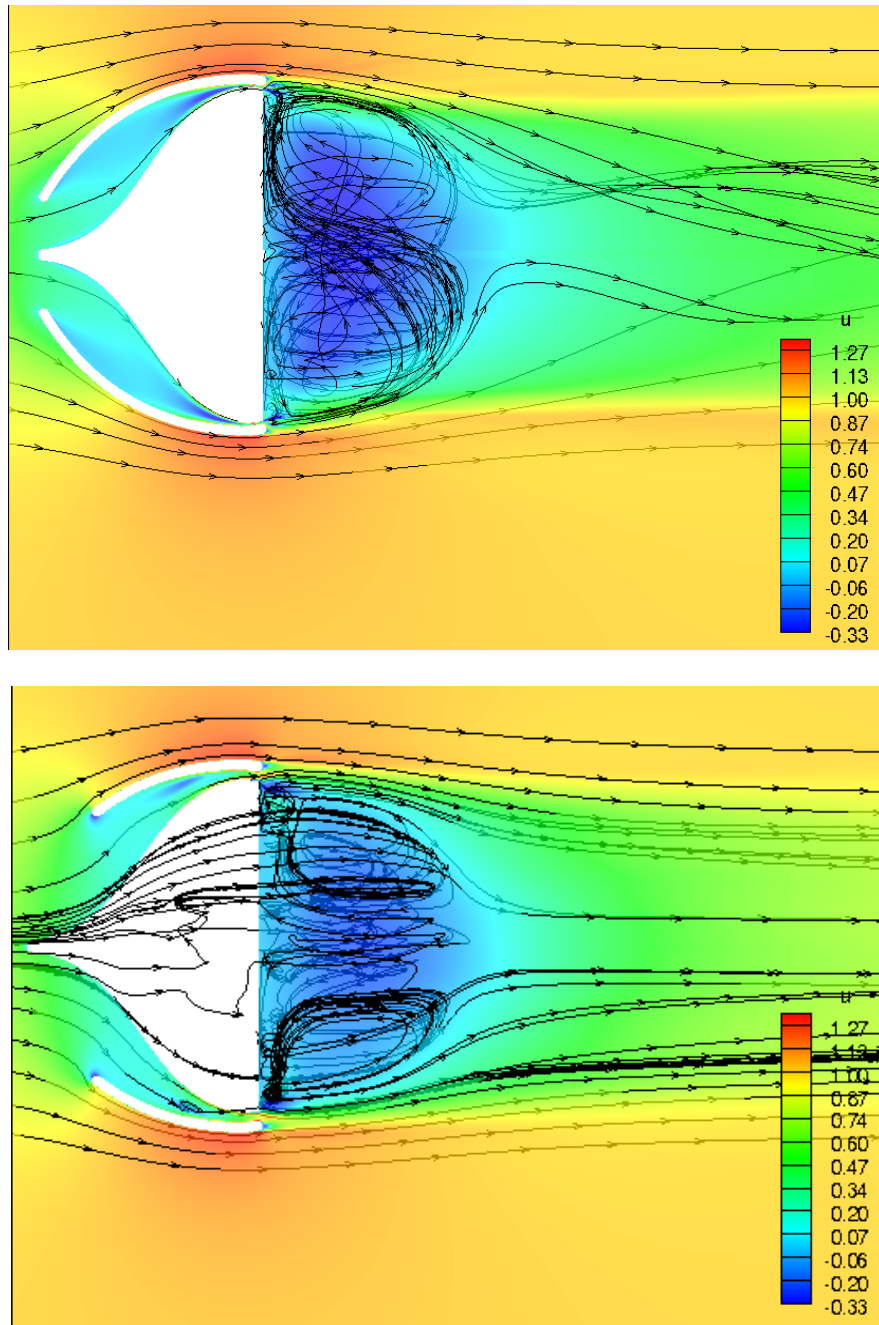
Fig. 33: Averaged High Reynolds Velocity Component Contours
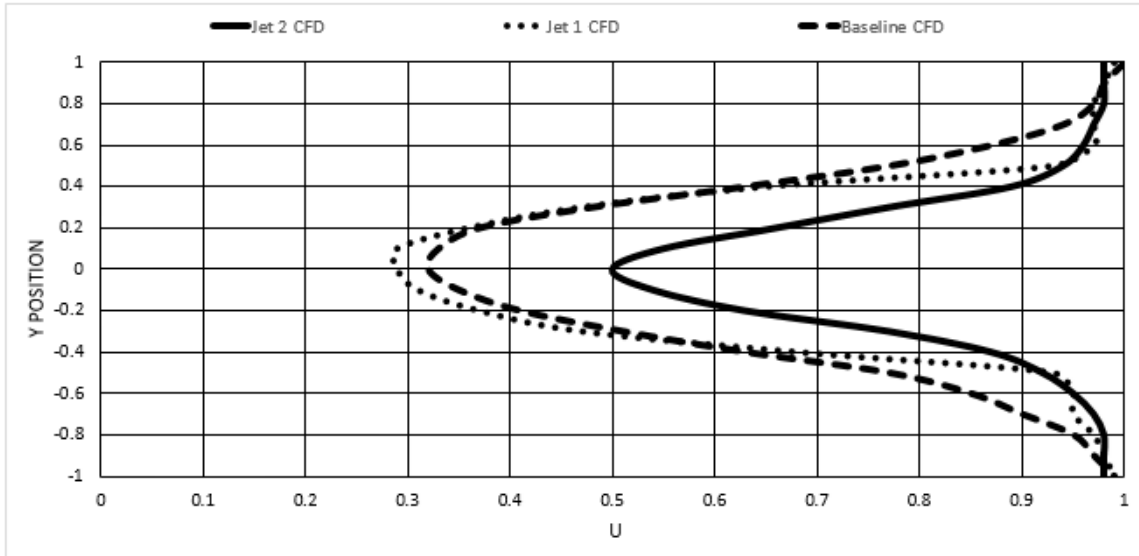
Figure 34: High Reynolds Downstream Component Plot (CFD)

In terms of the wake profiles the numerical results and contours are extremely alike. The same kind of wake area measurements, again averaged over 100t, are taken as seen in the previous Table 3.

High Reynolds	Wake Area	% Reduction
Jet 2	0.321	46.50%
Jet 1	0.552	8.00%
Baseline	0.6	

Table 7: High Reynolds Wake Area Results
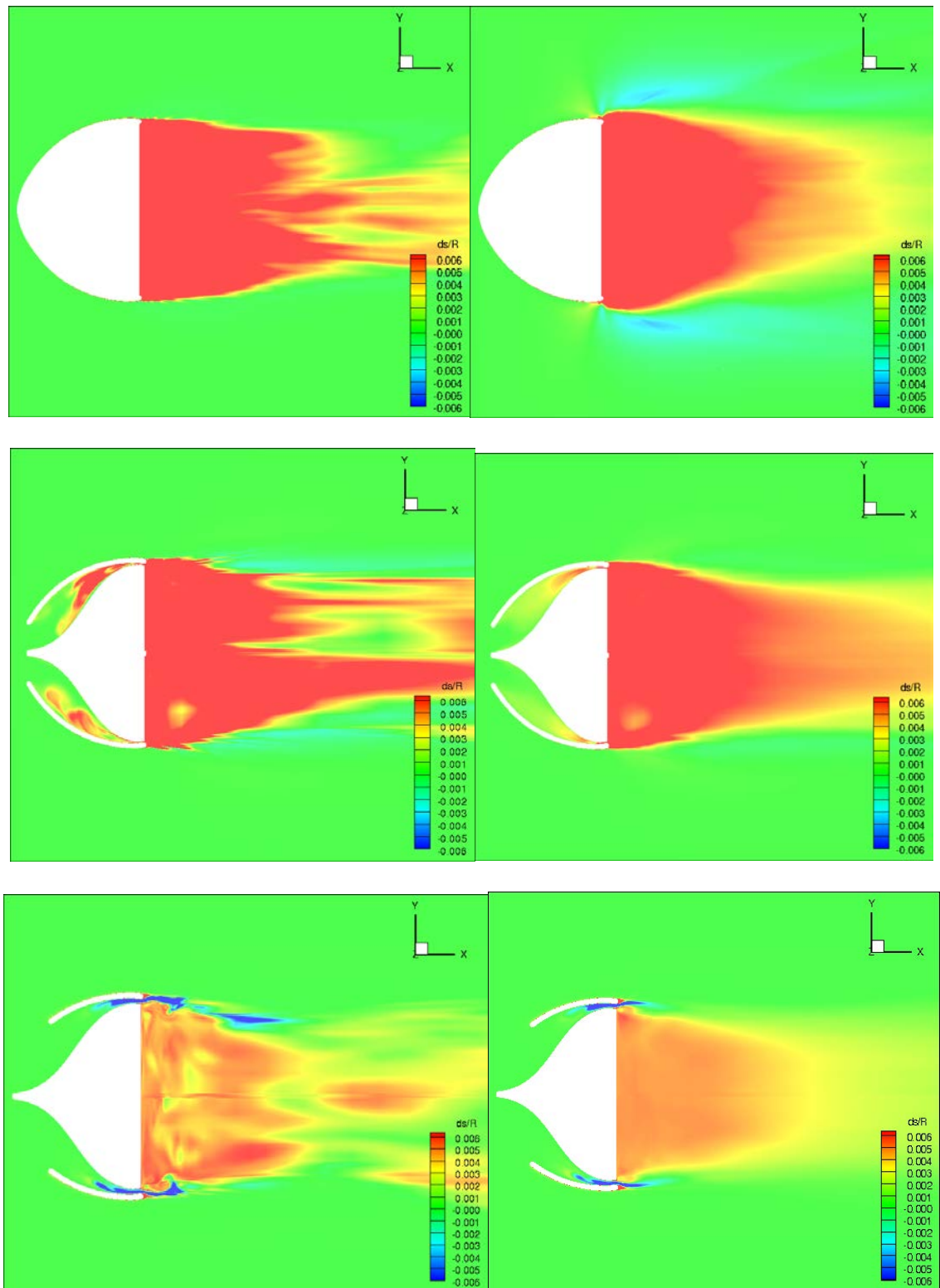
Fig. 35: High Reynolds Entropy Contours

The above high Reynolds entropy contours are similar to low Reynolds plots, with the

instantaneous plot on the left and time averaged plot on the right. The jet 2 case still

shows the negative entropy energizing jet.
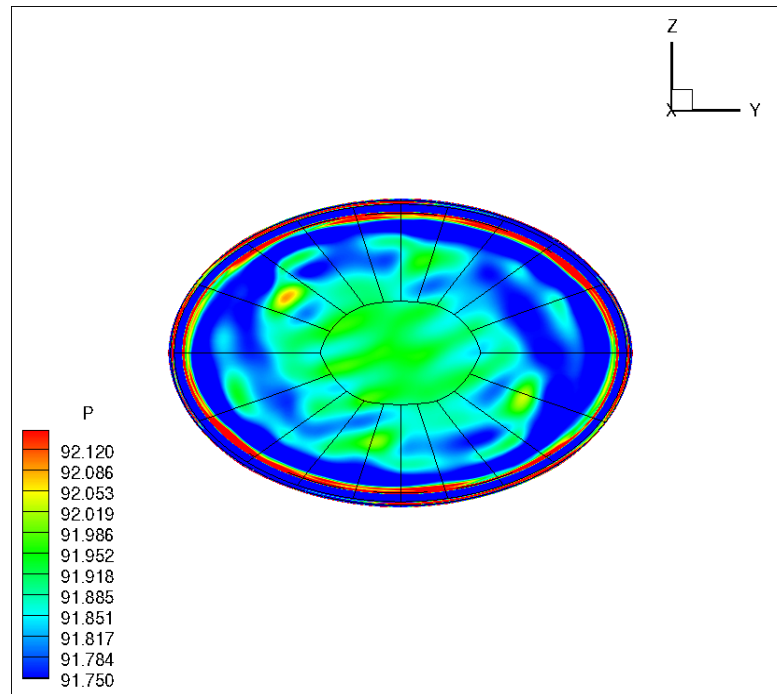
Fig. 36: High Reynolds Averaged Baseline Surface Pressure Contours
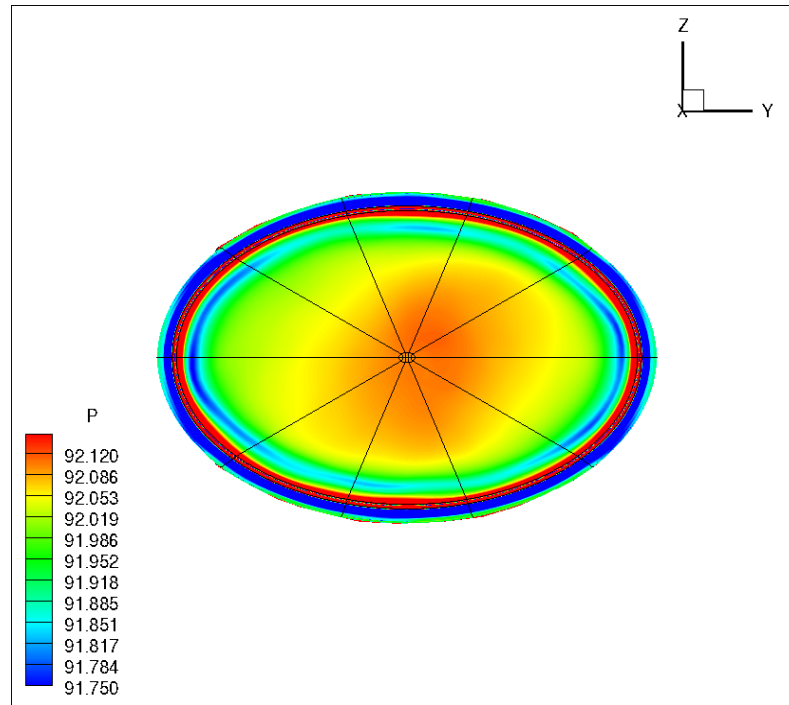
Fig. 37: High Reynolds Averaged Jet 1 Surface Pressure Contours
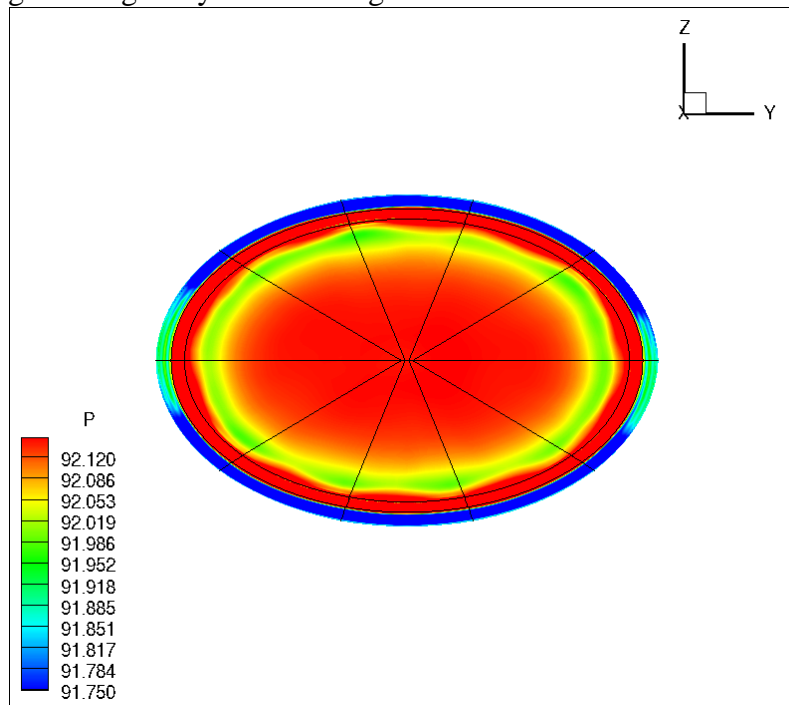
Fig. 38: High Reynolds Averaged Jet 2 Surface Pressure Contours

As seen in the above surface pressure figures the pressure on the base surface rises in the

jet models, thus drag reduction goes up significantly; and in all cases the Strouhal number

goes up by about 50%. Although wake reduction seems to be largely unaffected, the drag reduction of the jet mirror are still significant at a high Reynolds number.

Finally, if one estimates the drag contribution of the side-view mirror is 4% of the overall drag of the passenger automobile then, with jet 2 drag reduction, that 4% becomes 2.36%. Previous studies estimate that percentage drag reduction divided by two is equal to percent fuel reduction. Using this relation one can deduce that a car with jet 2 mirrors will consume .815% less fuel. This may seem like a tiny amount for a singular car, but if one extrapolates that percentage for all U.S. households, as a group there is about $10 billion in savings.

2.5 Result Comparison

Fig. 39 shows that the baseline mirror has vortex shedding in wind tunnel tests as well, clearly reflected as two counter rotating vortices of an average velocity field. This is an important distinction because vortex shedding is a component needed to prove the existence of base flow.
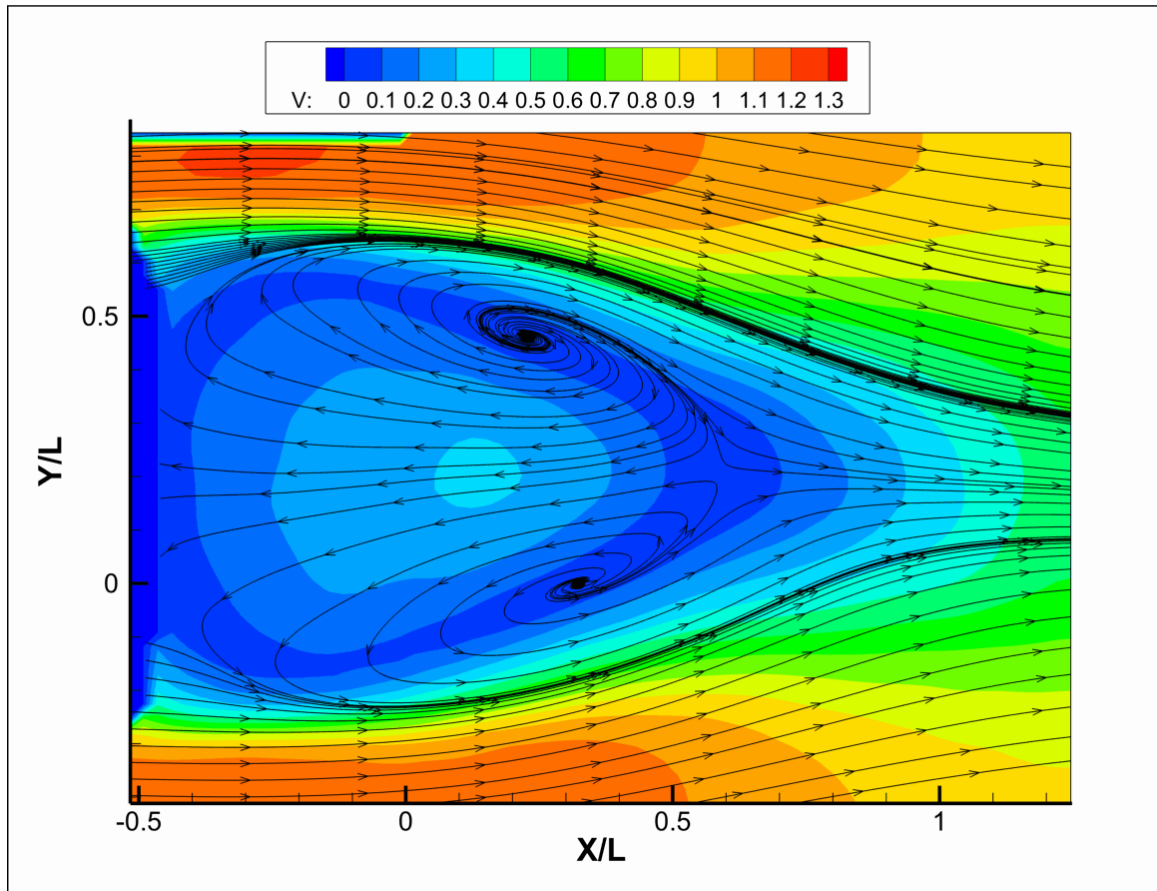
Fig. 39: Averaged PIV Baseline Velocity Contours

These averaged PIV results show that the wake area of jet 1 (Fig. 30) has a converging

shape and is narrower than the wake of the baseline model as expected.
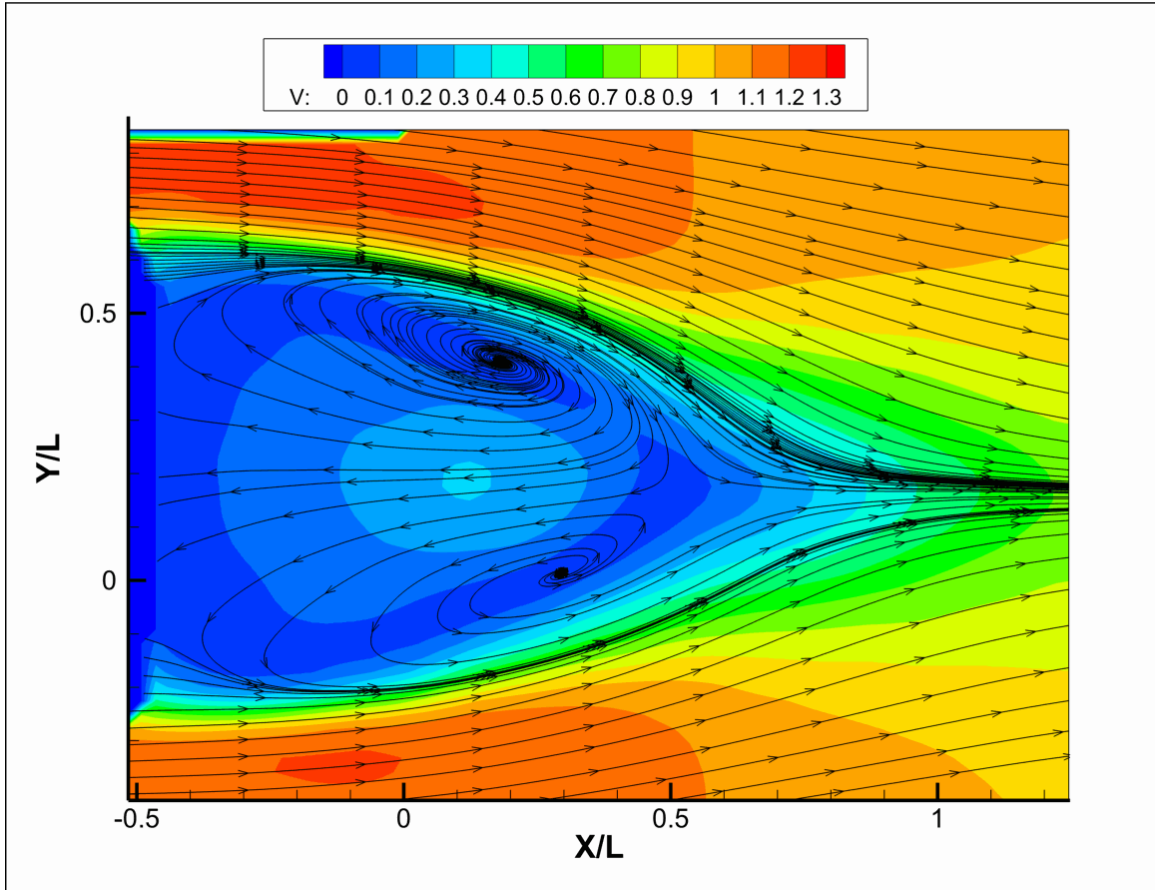
Fig. 40: Averaged Jet 1 Velocity Contours

The two vortices of the baseline mirror are seen further apart and the two vortices of the jet 1 mirror are closer to each other due to the reduced wake width. Finally, the jet 2 results are plotted in Fig. 41. The symmetric vortices are seen again, making them evident in all models, which proves the existence of base flow.
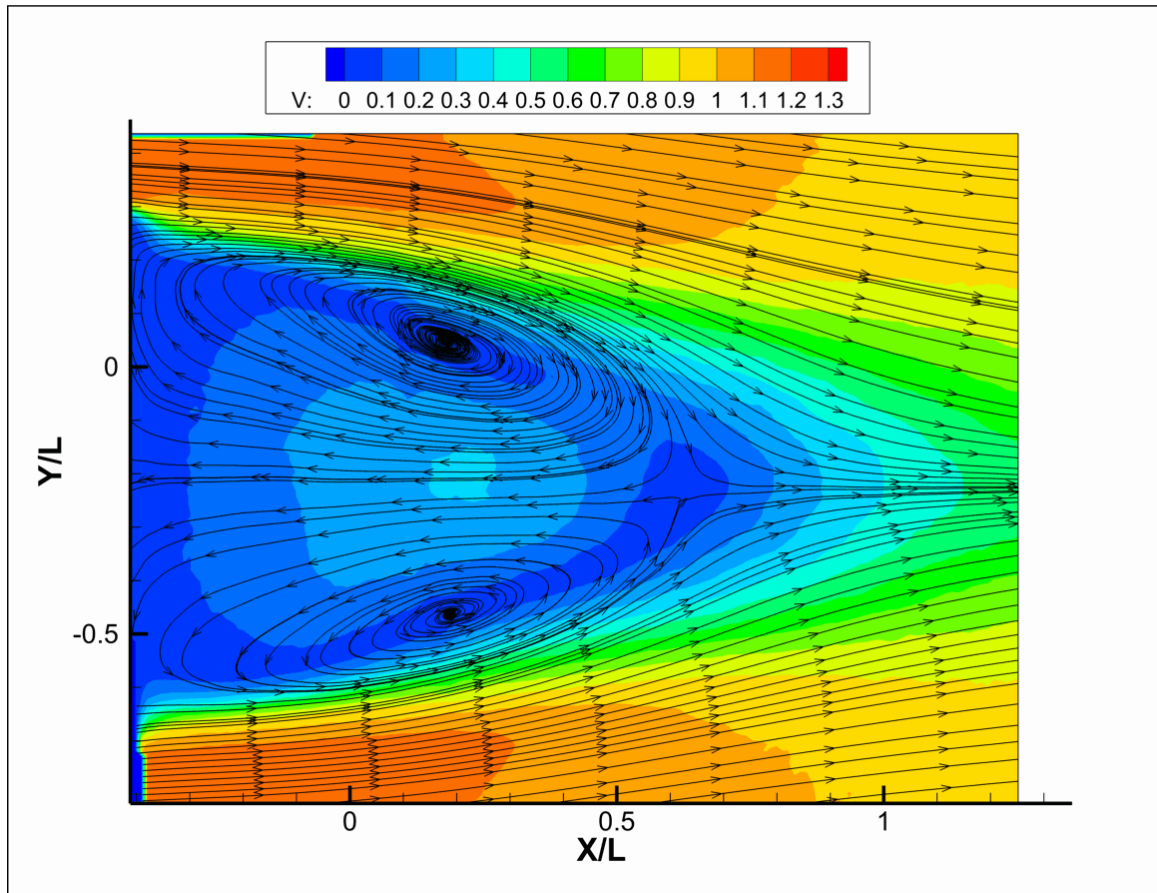
Fig. 41: Averaged PIV Jet 2 Velocity Contours

To confirm the reduced wake length, measurements of u (downstream velocity), are taken at 1.5 mirror lengths (Fig. 42) in accordance with the CFD wake measurements. Multiple points are taken on this line from the top of the mirror to the bottom of the mirror at its midsection. The points are plotted:
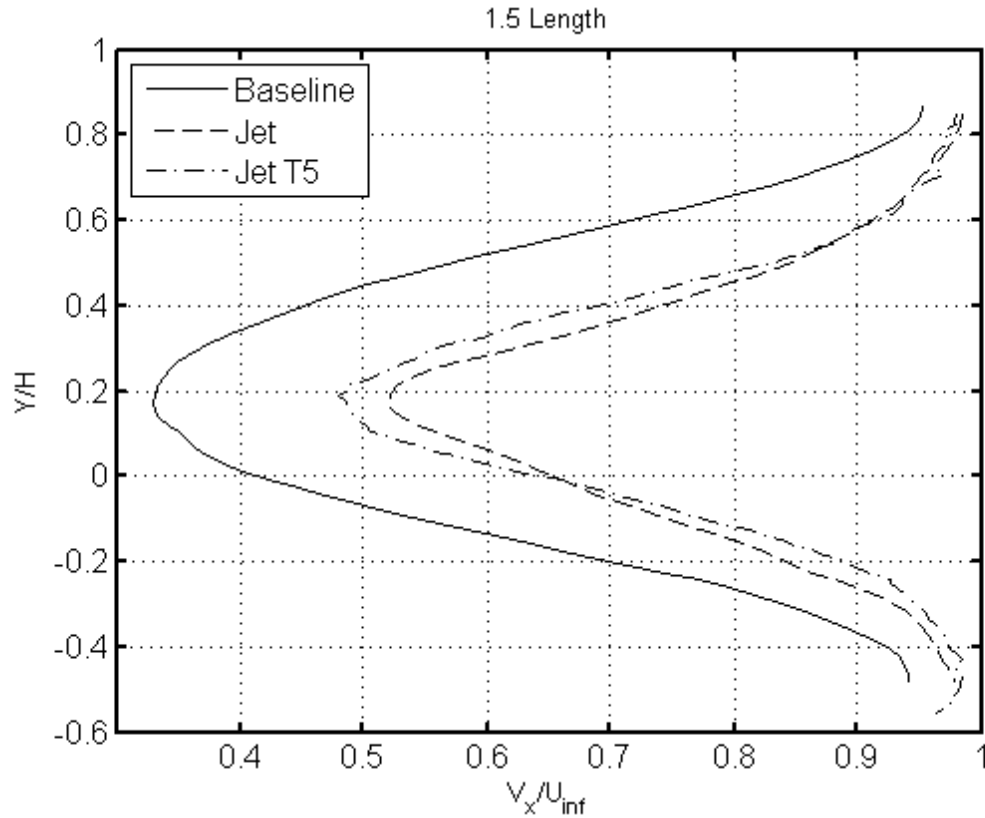
Fig. 42: Downstream Velocity Component Plot (Wind Tunnel)

The y-axis represents normalized vertical position and the x-axis is the downstream velocity divided by the free stream velocity. It can be observed that at 1.5 mirror lengths downstream the flow in the wake of the jet mirror is closer to free stream conditions than the flow in the wake of the baseline mirror. One can conclude that the wake of the jet mirror is slimmer and shorter. The smaller wake area of the jet 1 model conforms to the CFD results. In comparing the CFD and wind tunnel wake profiles there are a few obvious differences.
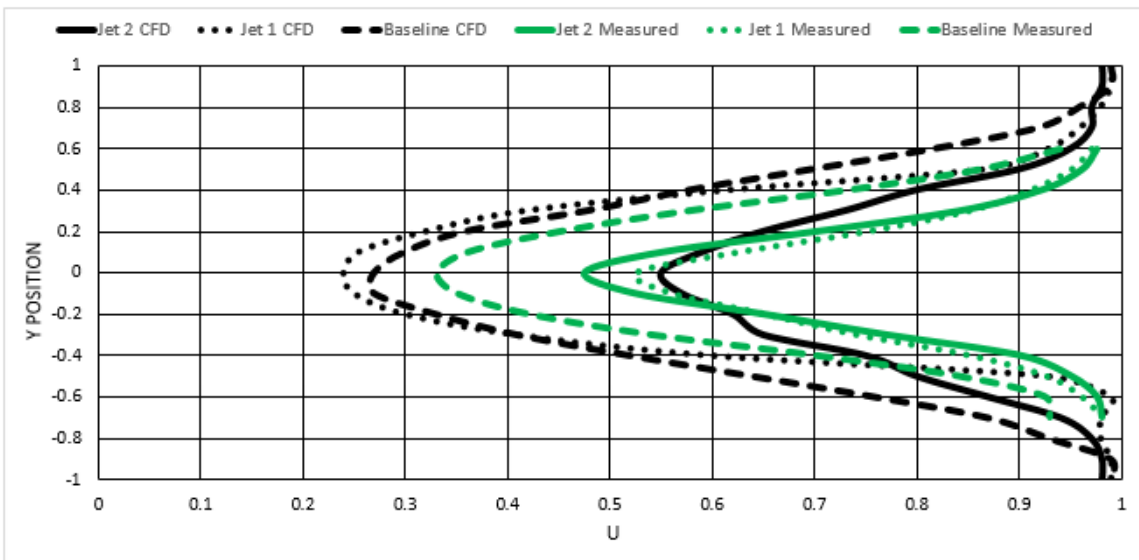
Fig. 43: Low Reynolds Downstream Velocity Component Plot Comparison

One, in the CFD results, the jet 1 wake length seems to be analogous to the baseline wake

length, while the wind tunnel measurements show a greatly reduced wake length between

the jet 1 and baseline models. Two, the CFD plots show a huge gap in length between jet

1 and jet 2. On the other hand, the wind tunnel plots say there is little difference in terms

of wake size between jet 1 and jet 2. In comparing the contour results (Fig. 34) these

differences become more visually evident. These wake results lead to the belief that

there may be differences in drag coefficient results.
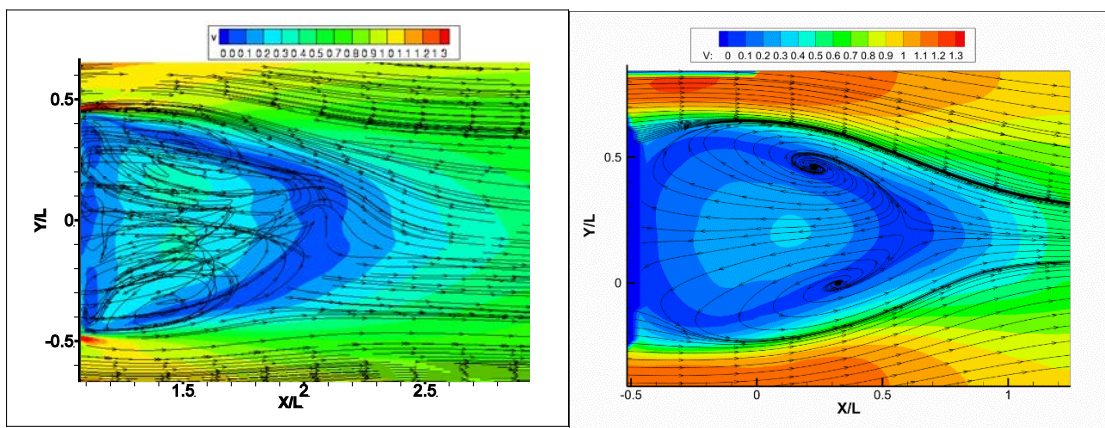
Baseline
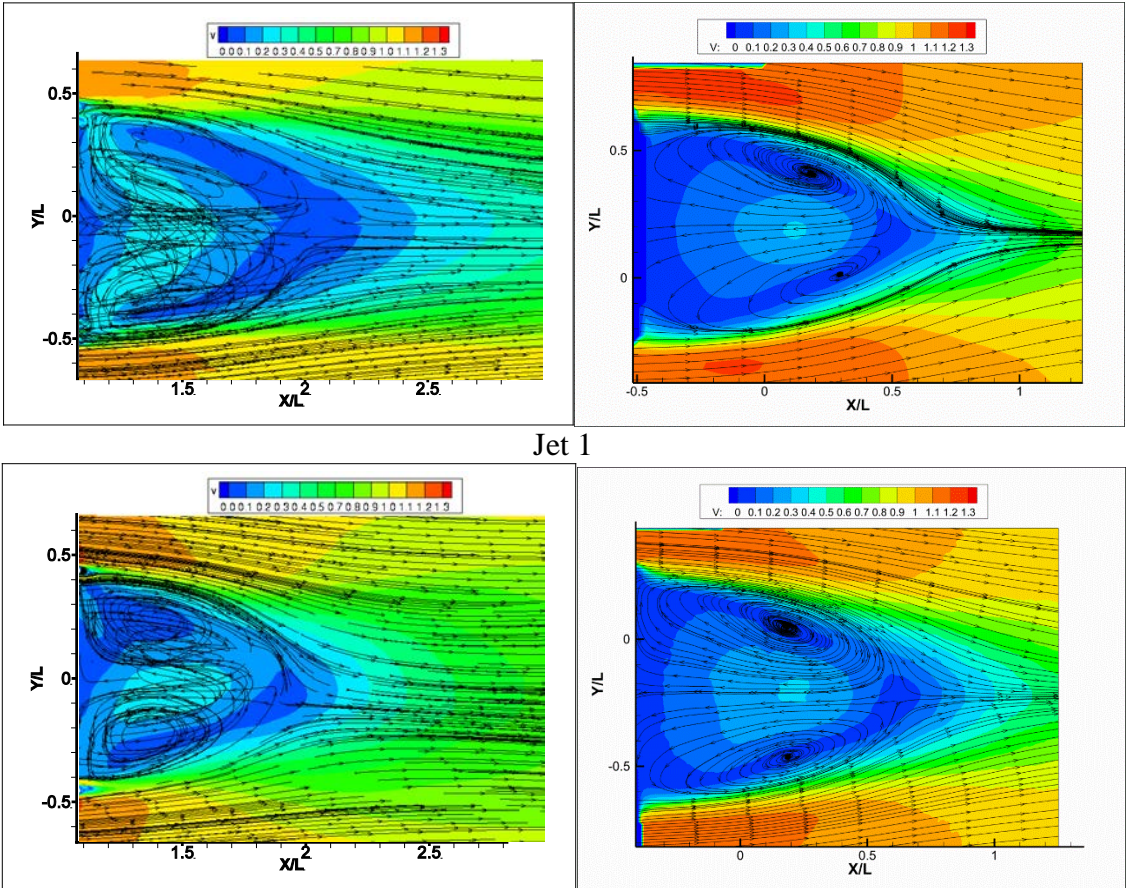
Jet 1

Jet 2
Fig. 44: Velocity Component Comparison Contours

Reynolds stress measurements were also taken in the wind tunnel. The comparison with CFD results is seen below:
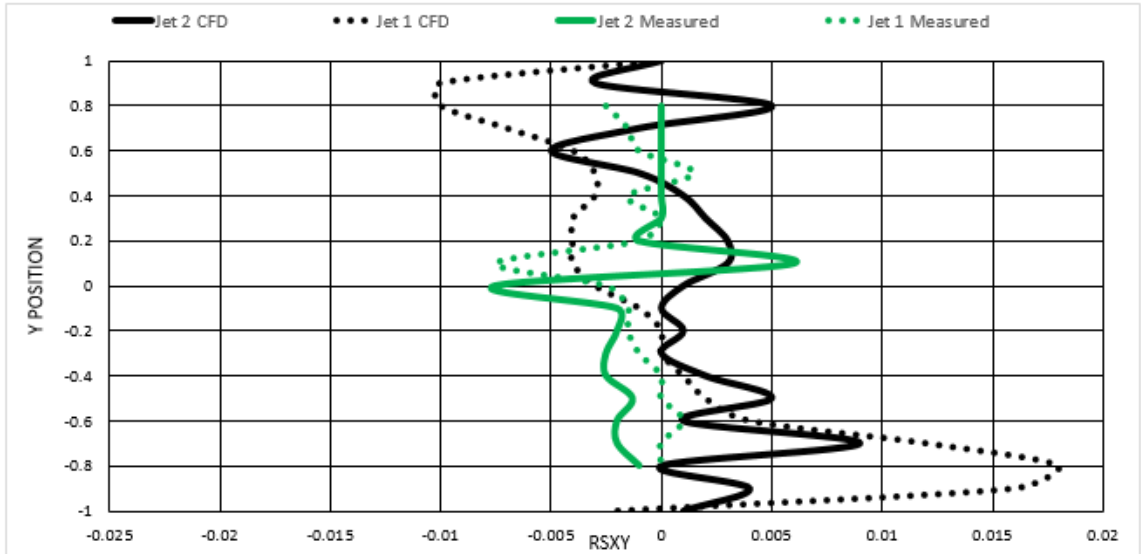
Figure 45: Reynolds Stress Comparison Plot

While the patterns of between measured and CFD results do not quite match up it is encouraging to see the values in each case are on the same order.

Fig. 46 shows the instantaneous flow visualizations of jet 1 without the streamlines and without velocity contours. It is clear that the jet is sucked upward by the mainstream even though the jet has a seven degree angle toward the center axis of the mirror. In Fig. 47, the jet mixing with the main flow creates clear large coherent vortex structures, which entrains the main flow to the base flow and energizes it. The overall effect is that the wake boundary is brought toward the centerline of the mirror and the wake becomes narrower. This gives strong indication that the jet mirror works as hypothesized.
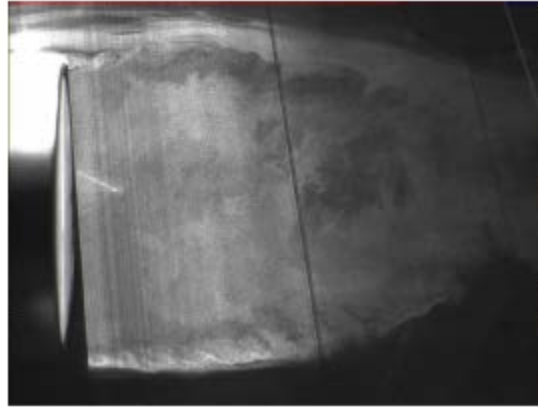
Fig. 46: Jet 1 Flow Visualization
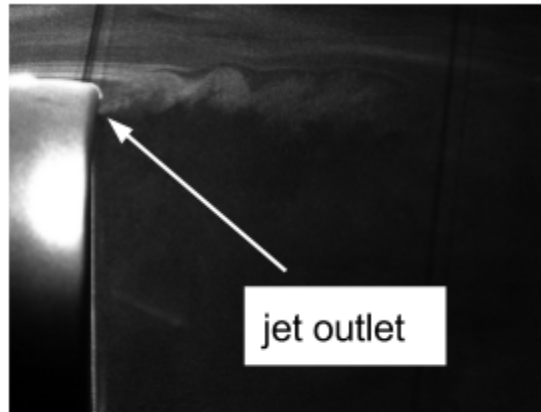
Fig. 47: Jet 1 Zoomed Flow Visualization

The drag force measurement experiments are performed in an open-jet closed circuit low speed wind tunnel at North Western Polytechnical University of Xian, China. The turbulivity of the wind tunnel is lower than 0.02%, meaning there is very little turbulence in the free stream [14]. All mirror models were tested at free stream velocity from 15 m/s to 40 m/s with a Reynolds number of 2.6×10^5 based on the length of the mirror. The drag results discussed in this thesis are those with free stream velocity equal to 30 m/s for both CFD and wind tunnel measurements.

The balance that measured drag force has a maximum of 80N and the error of the balance

is 0.02% of the full scale. The drag data acquired is at the frequency of 100 KHz and the

results given in this paper are averaged over a 30 second testing time. Table 7 shows the

complete comparison between CFD and wind tunnel measurements.

CFD				Wind Tunnel		
	Cd	Drag Reduction			Cd	Drag Reduction
Jet 2	0.26	40.91%	Jet 2		0.21	27.77%
Jet 1	0.34	29.41%	Jet 1		0.25	15.42%
Baseline	0.44		Baseline		0.3	

Table 8: CFD and Wind Tunnel Drag Coefficient Results

Chapter 3

Conclusion

Large Eddy Simulation is conducted to simulate the passive jet flow control for automotive mirror base drag reduction at Reynolds number of 2.6 x 10^5. This novel drag reduction method for automotive mirrors using passive jet flow control is demonstrated to be very effective by both wind tunnel testing and LES CFD simulation. Two jet mirrors, one with a large inlet and one with a small inlet are studied. The jet 1 has the inlet area that is 10% of the mirror base area, and the jet 2 has a 4.7 times larger inlet area. The drag reduction percentage agrees with the wind tunnel data, giving credence to both sets of results. As a trend the drag reduction predicted agrees with the experiment, specifically the LES predicts a significant drag reduction, up to 41%. The wind tunnel flow visualization and CFD show that the jet from the mirror is sucked upward due to the high total pressure of the jet. The jet mixing with the main flow creates large coherent vortex structures, which entrains the main flow to the base flow, energizing the base flow, reducing the wake size, turbulence fluctuation and most importantly drag. Overall qualitative flow field simulations agree well with the experimental PIV measurement. For jet mirror 1, the wake profile predicted is significantly deeper than the experiment. For jet mirror 2, the wake profile agrees very well with the PIV measurement with the wake area reduced by about 45%.

An unexpected phenomenon is discovered by the LES that the passive jet is energized with negative entropy. It makes the passive jet flow control similar to active jet flow control. The exact mechanism is not understood yet and further investigation is needed. The high Reynolds number flow is also simulated at Re= 2.6 x 10^6 to mimic the

effect for large road vehicles such as heavy duty trucks. Even though the qualitative phenomena are about the same as the low Reynolds number flows, the LES indicates that the drag reduction effect is greater at high a Reynolds number than at a low Reynolds number.

The use of passive flow jet control for base drag reduction is new and many future studies are needed. The following are some task that warrant investigation: LES with refined grid to resolve the wake better in order to match the experimental PIV measurements, study the effect of different jet flow angle, study the inlet and outlet ratio effect on the mixing and entrainment, and scaling for the drag reduction with the geometric parameters.

Appendix I

```
1000000, 0    !bc_max  the maximum of the BCs number defined in
problem

  50, 29500    !nb  the total number of blocks
  50,98,10     !il,jl,kl  the density of the grid of each block
  50,98,10     !il,jl,kl  the density of the grid of each block
  50,98,10     !il,jl,kl  the density of the grid of each block
  50,98,10     !il,jl,kl  the density of the grid of each block
  50,98,10     !il,jl,kl  the density of the grid of each block
  50,98,10     !il,jl,kl  the density of the grid of each block
  50,98,10     !il,jl,kl  the density of the grid of each block
  50,98,10     !il,jl,kl  the density of the grid of each block
  50,98,10     !il,jl,kl  the density of the grid of each block
  50,98,10     !il,jl,kl  the density of the grid of each block
  98,98,10     !il,jl,kl  the density of the grid of each block
  98,98,10     !il,jl,kl  the density of the grid of each block
  98,98,10     !il,jl,kl  the density of the grid of each block
  98,98,10     !il,jl,kl  the density of the grid of each block
  98,98,10     !il,jl,kl  the density of the grid of each block
  98,98,10     !il,jl,kl  the density of the grid of each block
  98,98,10     !il,jl,kl  the density of the grid of each block
  98,98,10     !il,jl,kl  the density of the grid of each block
  98,98,10     !il,jl,kl  the density of the grid of each block
  98,98,10     !il,jl,kl  the density of the grid of each block
  50,98,10     !il,jl,kl  the density of the grid of each block
  50,98,10     !il,jl,kl  the density of the grid of each block
  50,98,10     !il,jl,kl  the density of the grid of each block
  50,98,10     !il,jl,kl  the density of the grid of each block
  50,98,10     !il,jl,kl  the density of the grid of each block
  50,98,10     !il,jl,kl  the density of the grid of each block
  50,98,10     !il,jl,kl  the density of the grid of each block
  50,98,10     !il,jl,kl  the density of the grid of each block
  50,98,10     !il,jl,kl  the density of the grid of each block
  50,98,10     !il,jl,kl  the density of the grid of each block
  50,98,10     !il,jl,kl  the density of the grid of each block
  50,98,10     !il,jl,kl  the density of the grid of each block
  50,98,10     !il,jl,kl  the density of the grid of each block
  50,98,10     !il,jl,kl  the density of the grid of each block
  50,98,10     !il,jl,kl  the density of the grid of each block
  50,98,10     !il,jl,kl  the density of the grid of each block
  50,98,10     !il,jl,kl  the density of the grid of each block
  50,98,10     !il,jl,kl  the density of the grid of each block
  50,98,10     !il,jl,kl  the density of the grid of each block
  50,129,10    !il,jl,kl  the density of the grid of each block
  50,129,10    !il,jl,kl  the density of the grid of each block
  50,129,10    !il,jl,kl  the density of the grid of each block
  50,129,10    !il,jl,kl  the density of the grid of each block
  50,129,10    !il,jl,kl  the density of the grid of each block
  50,129,10    !il,jl,kl  the density of the grid of each block
  50,129,10    !il,jl,kl  the density of the grid of each block
  50,129,10    !il,jl,kl  the density of the grid of each block
```

```
50,129,10      !il,jl,kl  the density of the grid of each block
50,129,10      !il,jl,kl  the density of the grid of each block
0              !The number of additional poutlet condit
```

Appendix II

```
&consts
delta           = 0.0d+00, 0.0d+00, 0.0d+00, 0.0d+00, 0.0d+00,! Entropy
cut-off
                               ! for rho, rhou, rhov, rhow and rhoe
respectively
epsfactor       = 1.00d-06, ! epsilon used in linear reconstruction
gamma           = 1.40d+00, ! Ratio of specific heats
prandtl         = 0.72d0,   ! Molecular Prandtl number
prt             = 0.9d0,    ! turbulent prandtl number
suther          = F,        ! = T: Sutherlands Law; = F: mu = T
tref            = 0.377d0,  ! Non-dimensional ref temperature in
Sutherland
/

&flows
blen            = 3,        ! the number of halo layers for block
boundaries.
                               ! =2, under 3rd scheme;
                               ! =3, 5th scheme;
                               ! =4, 7th scheme
idimen          = 3,        ! = 1: 1-D, = 2: 2-D, = 3: 3-D
nl              = 5,        ! No. of eqs.
                               ! =5, Laminar or BL model;
                               ! =6, SA model or DES
angl1           = 0.d0,     ! inlet angle 1
angl2           = 0.d0,     ! inlet angle 2
inviscid        = F,        ! = T: inviscid;
                               ! = F: viscous
machinf         = 0.088d0,  ! Mach no. based on U_infinity and
a_infinity
reynolds        = 2.60d5,   ! Reynolds number
poutlet         = 92.23731, ! outlet static pressure
ptotal          = 92.73828, ! Total pressure at inlet
ttotal          = 1.001549, ! Total temperature at inlet
tintvl          = 0.02,     ! unsteady time interval
turb            = 0,        ! =0, Laminar flow or LES without SGS
                               ! =1 (nl=5), BL turbulence model;
                               ! =1 (nl=6), SA turbulence model or DES
                               ! =4 LES with SGS
ns              = 1,        ! Species Number. (For Navier-Stokes eq,
ns=1)
                               ! if ns>1, please modify namelist &chemistry
nr              = 0,        ! Chemical reaction number. (=0, no
Chmistry)
mhd             = 0,        ! =0, without Magnetohydrodynamics
                               ! =3, with magnetohydrodynamics
psvscl          = 0,        ! =0, no passive scalar
                               ! =1, one passive scalar
```

```
                /

                &comp
                choice      = 'y',       ! ='y': from rstore.
                                         ! ='n': from initial value
                cfl         = 1.5d0      ! CFL number
                unidt       = 0,         ! >0, Uniform time interval in whole domain
                                         ! =0, Local time step
                intersteps  = 500,       ! save results every # steps in computation
                nstep       = 30000,     ! No. of time steps
                integrate   = 4,         ! =1, AF;
                                         ! =2, R-K;
                                         ! =3, Euler;
                                         ! =4, GS;
                                         ! =5, LU-SGS;
                                         ! =6, LU-GSLR
                iter_gs     = 2,         ! number of Gauss-Seidel sweeps
                lhs_order   = 0,         ! =0, 1st order MUSCL for LHS matrices
                (suggested);
                                         ! =1, 2nd or 3rd order.
                lhs_scheme  = 1,         ! =1, Roe; (suggest use "1" when
                preconditioning >=1)
                                         ! =2, Zha;
                                         ! =3, none,
                                         ! =4, Van Leer (when RHS is not Roe scheme)
                rhs_scheme  = 1,         ! 1:Roe;
                                         ! 2:Zha2;
                                         ! 3:Zha3;
                                         ! 4:VLeer;
                                         ! 5:Edwars;
                                         ! 6:Zha6;
                                         ! 7:AUSM+;
                                         ! 8:Zha;
                                         ! 9:AUSMV;
                                         ! 10:AUSMD;
                                         ! 11:VLEER-HANEL
                                         ! 33: ECUSP + Van Leer (based on Edwards JCP
                1996,
                                         !     123:84-95, Hypersonic chemical flow)
                                         ! 82: Rotated ZHA ECUSP+Rusanov
                                         ! 83: Rotated ZHA ECUSP+HLL
                                         ! 86: Rotated Roe + Rusanov
                                         ! 87: Rotated Roe + HLL
                                         ! 100: Steger Warming FVS (not finished)
                                         ! NOTE: 82-87 are suggested for Hypersonic
                Blunt body
                                         !    83 and 87 are better than 82 and 86,
                respectively
                rhs_order   = 1,         ! =0, 1st order MUSCL (blen>=2);
                                         ! =1, 2nd or 3rd order (blen>=2);
                                         ! =4, 3rd-WENO (blen>=2);
                                         ! =5, 5th order fixed stencil (blen=>3);
                                         ! =6, 5th-WENO (blen=>3);
```

```
                             ! =106, Borges 5th-WENO(blen=>3);
                             ! =116, 5th-WENO improved near
shock(blen=>3);
                             ! =206, Martin's 6th-WENO(blen=>3);
                             ! =7, 7th order fixed stencil (blen=>4);
                             ! =8, Balsara and Shu's 7th-WENO (blen=>4)
                             ! =108, Shen and Zha's 7th-WENO (blen=>4)
                             ! =455, finite-compact, (Borges
WENO5+Pade6)(blen=>3)
limiter     = 0,            ! NOTE: limiter only used when rhs_order=1
                             ! =0, no limiter;
                             ! =1, MINMOD ;
                             ! =2, SUPERBEE;
                             ! =3, A-T-VL
kfactor     = 0.33333d0,    ! factor in MUSCL linear reconstruction,
                             !       only used when rhs_order=1
dual_t      = 1,            ! 1: unsteady,
                             ! 0: steady
tsteps      = 30,           ! used for unsteady calculation
                             ! unsteady time marching steps using dual-
time stepping
moving      = 0,            ! moving grid,
                             ! 0-stationary,
                             ! 1-fixed,
                             ! 2-induced
strtp       = 0,            ! 0-no structure;
                             ! 1-cylinder;
                             ! 2-airfoil
gcl         = 0,            ! geometry conservation law for moving grid
(0,1)
eps         = 1.d-12,        ! residual limit
checksteps  = 1,            ! print out status every # steps for
monitoring
nrbc_ex     = 0,            ! =0: no NRBC at exit;
                             ! =3: use Euler Method NRBC at exit
sigma       = 0.25,         ! coefficients for NRBC
vis_order   = 1,            ! The order of the viscous term. Only for
viscous flow
                             !   =1, 2nd order(blen=2);
                             !   =3, 4th order(blen=3);
                             !   =5, 6th order(blen=4)
strm_dir    = 1,            ! main flow direction
                             !   =1, u=velinit, v=0, w=0
                             !   =2, v=velinit, u=0, w=0
                             !   =3, w=velinit, u=0, v=0
                             !   =4, blasius solution (flate plate)
velinit     = 1.d0,         ! dimensionless velocity initial value
theta       = 0.d0,         ! initial velocity angle
twpar       = 2,            ! 1<=twpar<=10, initial for omega when nl=7
tkpar       = 5,            ! 2<=tkpar<=5, initial for k when nl=7
precondition= 0,            ! 0, no preconditiong
                             ! =1, precondition (gas)
                             ! =2, preconditioning (water)
prim_var    = 1,            ! for preconditioning methods
```

```
                          ! =1, (p,u,v,w,T)
                          ! =2, (rho,u,v,w,T)
k_prec      = 0.75        ! only used for preconditioning methods, can
be changed
source      = 0,          ! =0, neglect gravity source term
                          ! =1, gravity source term, please modify
&source_g
varepsilon = 1e-2,        ! can be changed
                          ! used for WENO scheme (original is 1e-6),
                          ! in constructing weights, to aviod a/0
                          ! proper value can improve accuracy and
convergence
wall_order = 1,           ! accuracy on wall
                          ! 1----1st order;
                          ! 3----3rd order
tbl_average = 1,          ! for turbulent statistical values
                          ! =0, do not need turbulent averaged values
                          ! =1, need turbulent averaged values
newgrid     = 0,          ! =1, Use new grid in case choice 'y'
                          !   only mesh changed and wnt to use the old
flowfield
                          !   read the new mesh from bin-files, same
dimension
                          ! =0, Use initial grid
Tfrozen     = 500,        ! (K), under this value(temperature),
                          !     there is no chemical reaction
chem_step   = 100,        ! chemical reaction time steps in one flow-
step
rotide      = 0,          ! for rotor: IF >=1, please modify &rotor
                          ! = 0 no frame rotating
                          ! =1  rotor 37
                          ! =2, rotor67
                          ! =3, ge-rotor
                          ! =4, honeywell rotor
                          ! =5, general rotor and multistage(uniform
inlet prfoile)
multistage  = 0,          ! only used when rotide>0
                          ! =0, single rotor
                          ! =1, multi-stage
schmidt     = 0.0,        ! schmidt number
cfj      = 0,           ! activate cfj mass flow regulation
movie    = 0,           ! activate the movie special recording feature
in mymovie namelist
cflramp     = 0,          ! activate the CFL ramp in mycfl namelist
initype     = 0,
helcop      = 0,
mirror      = 3,          ! 0=none, 1=base, 2=tunnel1, 3=tunnel5
/

&coef1eq
ides    = 0,            ! =0, 1EQ; =1, DES
cdes    = 0.65d0,       ! parameter used in DES
iblnu   = 1,            ! block number in which trip is placed
ipt     = 1,            ! index of trip point in i-direction
```

```
jpt     = 1,               ! index of trip point in j-direction
kpt     = 1,               ! index of trip point in k-direction
ic1     = 1,               ! ic1, ic2 and ic3 represent the i, j, k
grid
ic2     = 0,               ! spacing along the wall at the trip.
ic3     = 0,               ! =0, no the direction; =1, along the
direction
tko   = 0.66666667d0,     ! constant used in SA 1EQ turbulence model
cb1   = 0.1355d0,         ! constant used in SA 1EQ turbulence model
cb2   = 0.622d0,          ! constant used in SA 1EQ turbulence model
cap_k = 0.41d0,           ! constant used in SA 1EQ turbulence model
cw2   = 0.3d0,            ! constant used in SA 1EQ turbulence model
cw3   = 2.d0,             ! constant used in SA 1EQ turbulence model
cv1   = 7.1d0,            ! constant used in SA 1EQ turbulence model
ct1   = 0.0d0,            ! constant used in SA 1EQ turbulence model
ct2   = 0.0d0,            ! constant used in SA 1EQ turbulence model
ct3   = 0.0d0,            ! constant used in SA 1EQ turbulence model
ct4   = 0.0d0             ! constant used in SA 1EQ turbulence model
/

&clcd
lref    = 12.9d0,        ! reference length
aref    = 188.79d0,      ! reference area, this aref should refer to
the power of lref
xref    = 0.d0,          ! x-coordinate of reference point
yref    = 0.d0,          ! y-coordinate of reference point
ifaf    = 0,             ! =0: only output cl and cd; =1: cl,cd
transfter to axial and normal force
afa     = 0.d0           ! angle between free stream and axis of
body, use with 'ifaf', if ifaf=0, afa=0.0 output cl and cd only
                         ! if the meshes are already rotated and
ifaf=1, set afa according to your model and BC
/


&mvgrid2
xctr    = 0.d0,          ! x-coordinate of central point in grid re-
construction
yctr    = 0.d0,          ! y-coordinate of central point in grid re-
construction
jfx     = 10,           ! index for grid re-construction (when
j>jfx)
beta    = 1.0002d0 /     ! grid ratio used in grid re-construction


&strct_cyl
cs        = 0.1583d0,    ! parameters for induced vibration of
cylinder
mus       = 12.732395d0, ! parameters for induced vibration of
cylinder
ub        = 1.5915494d0  ! parameters for induced vibration of
cylinder
/
```

```
&mycfj
cmu_target = 8.0d-2        ! value of Cmu desired by the user
inj_prec    = 1.0d0        ! precision on injection mass flow
requested by user (%)
suc_prec    = 1.0d0        ! precision on suction mass flow
requested by user (%)
inj_ampli   = 8            ! injection pressure correction term
                           ! (the larger the term the smaller the
correction)
                  ! 8 for open slot, 15 for 2/3 CFJ
suc_ampli   = 40           ! suction pressure correction term
                           ! (the larger then term the smaller the
correction)
                  ! 40 for open slot, 20 for 2/3 CFJ
index       = 0            ! starting index for the mass flow
correction
cfjstep     =  1000        ! number of time step between
corrections
vref_cfj    = 102.9678     ! Reference velocity (m/s)
tref_cfj    = 293.15       ! Reference temperature (K)
roref_cfj   = 1.205d0      ! Reference density (kg/m3)
/


Boundary conditions:
Note: Boundary conditions
1      zero gradient
2      supersonic inflow
3      no slip adiabatic wall boundary
4      zero gradient with w = 0
5      subsonic outflow, fixed static pressure (poutlet in datain)
6      subsonic inflow, fixed rho, u, v, w at inlet
7      inner boundary for mpi
8      symmetry boundary
9      subsonic inlet BC with fixed total pressure and temperature
10     periodic boundary condtion
11     subsonic outflow, fixed static pressure (computed in code)
19     isothermal wall, zero-gradient pressure
20     periodic boundary condtion for flow variables only
31     partial-slip wall boundary in rotation coordinates
32     moving wall boundary
33     dpdn = 0 wall boundary in rotation coordinates
34     dpdn = 0, dtdn = 0, psi changes wall boundary in rotation
coordinates
35     dpdn = rv^2/r, dtdn = 0, wall boundary in rotation
coordinates
71     rotating periodic boundary conditio
95     special case: specify u=1, v=w=0 (eg. lid cavity), j-upper
boundary
100    special case: shock/boundary layer interaction, j-upper
boundary
***
```

```
101-110    isothermal wall, please modify the corresponding
temperature value
            (nondimensional temperature)
            in namelist &iso_t-------->iso_tw,
            For example, if in &bcdef bctype=105 is used ,
                          the value of iso_tw at ! 105 should change to
the
                          value you want, for example, 1.02, 12.5,...
======================================================================
====
Note: Initial flow profiles (strm_dir)
1       uniform flow
4       Blasius profile (especially for benchmark case: super flat
plate)
======================================================================
===
```

Appendix III

LOW REYNOLDS

JET 2

x={1,.9,.8,.7,.6,.5,.4,.3,.2,.1,0,-.1,-.2,-.3,-.4,-.5,-.6,-.7,-.8,-.9,-1}

{1,0.9,0.8,0.7,0.6,0.5,0.4,0.3,0.2,0.1,0,-0.1,-0.2,-0.3,-0.4,-0.5,-0.6,-0.7,-0.8,-0.9,-1}

y={.98,.98,.97,.97,.95,.9,.8,.73,.65,.59,.55,.57,.62,.65,.75,.8,.87,.94,.97,.98,.98}

{0.98,0.98,0.97,0.97,0.95,0.9,0.8,0.73,0.65,0.59,0.55,0.57,0.62,0.65,0.75,0.8,0.87,0.94,0.97,0.98,0.98}

ytest={1,1,1,1,1,1,1,1,1,1,1,1,1,1,1,1,1,1,1,1,1}

{1,1,1,1,1,1,1,1,1,1,1,1,1,1,1,1,1,1,1,1,1}

f=Interpolation[Transpose@{x,y}, InterpolationOrder→1]

InterpolatingFunction[{{-1.,1.}},<>]

Plot[f[t],{t,Min@x,Max@x},PlotRange→{0,1},Filling→Axis]
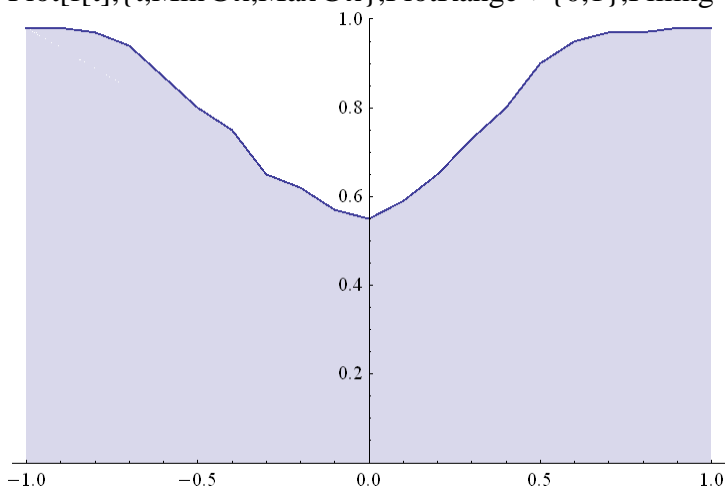
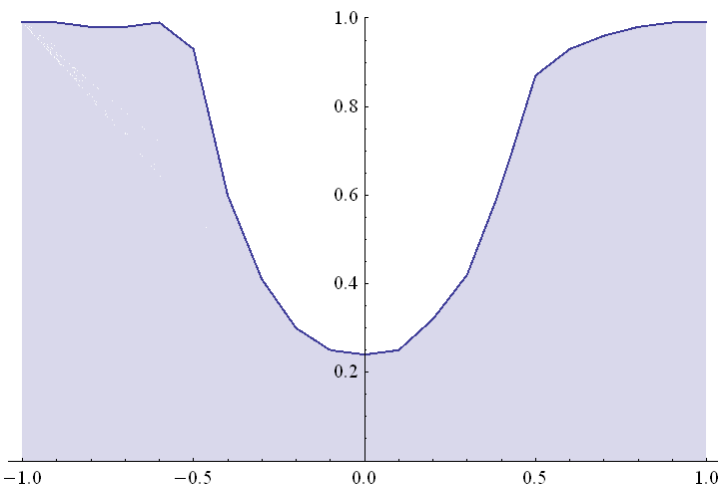
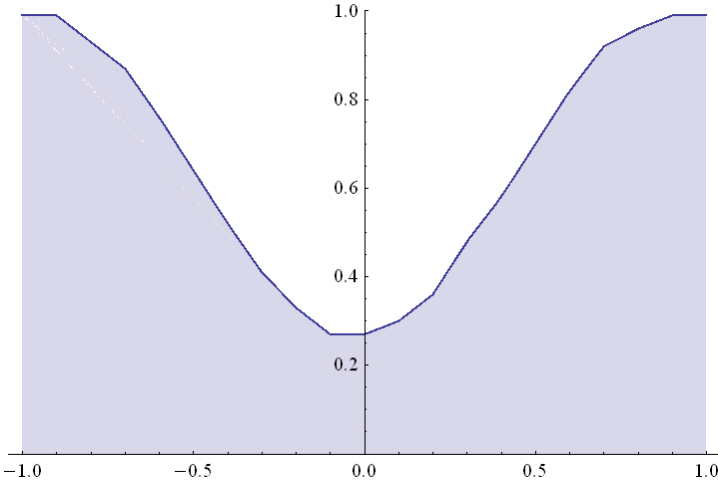NIntegrate[f[t],{t,Min@x,Max@x},Method→"LocalAdaptive"]

1.622

2-1.622

0.378

JET 1

y1={.99,.99,.98,.96,.93,.87,.62,.42,.32,.25,.24,.25,.3,.41,.6,.93,.99,.98,.98,.99,.99}

{0.99,0.99,0.98,0.96,0.93,0.87,0.62,0.42,0.32,0.25,0.24,0.25,0.3,0.41,0.6,0.93,0.99,0.98,0.98,0.99,0.99}

f=Interpolation[Transpose@{x,y1}, InterpolationOrder→1]

InterpolatingFunction[{{-1.,1.}},<>]

Plot[f[t],{t,Min@x,Max@x},PlotRange→{0,1},Filling→Axis]

NIntegrate[f[t],{t,Min@x,Max@x},Method→"LocalAdaptive"]

1.4

2-1.4

0.6

BASELINE

yb={.99,.99,.96,.92,.82,.7,.58,.48,.36,.3,.27,.27,.33,.41,.52,.64,.76,.87,.93,.99,.99}

{0.99,0.99,0.96,0.92,0.82,0.7,0.58,0.48,0.36,0.3,0.27,0.27,0.33,0.41,0.52,0.64,0.76,0.87,0.93,0.99,0.99}

f=Interpolation[Transpose@{x,yb}, InterpolationOrder→1]

InterpolatingFunction[{{-1.,1.}},<>]

Plot[f[t],{t,Min@x,Max@x},PlotRange→ {0,1},Filling→Axis]

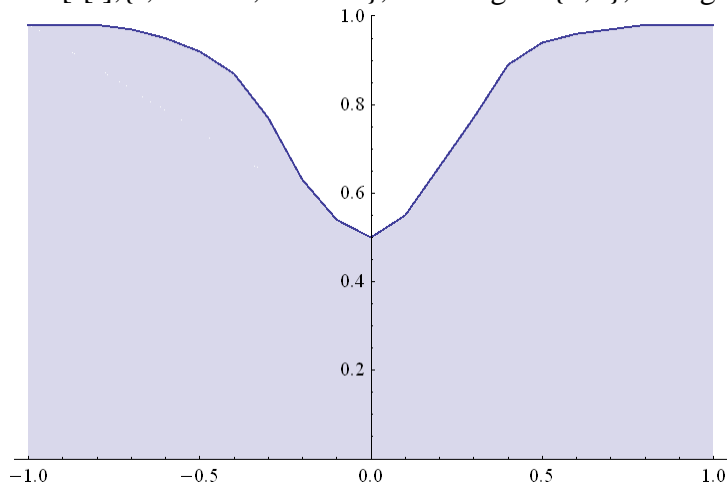NIntegrate[f[t],{t,Min@x,Max@x},Method→"LocalAdaptive"]

1.309

2-1.309

0.691

HIGH REYNOLDS

JET 2

x={1,.9,.8,.7,.6,.5,.4,.3,.2,.1,0,-.1,-.2,-.3,-.4,-.5,-.6,-.7,-.8,-.9,-1}

{1,0.9,0.8,0.7,0.6,0.5,0.4,0.3,0.2,0.1,0,-0.1,-0.2,-0.3,-0.4,-0.5,-0.6,-0.7,-0.8,-0.9,-1}

y={0.98,0.98,0.98,0.97,0.96,0.94,0.89,0.77,0.66,0.55,0.5,0.54,0.63,0.77,0.87,0.92,0.95
,0.97,0.98,0.98,0.98}

{0.98,0.98,0.98,0.97,0.96,0.94,0.89,0.77,0.66,0.55,0.5,0.54,0.63,0.77,0.87,0.92,0.95,0.97,
0.98,0.98,0.98}

ytest={1,1,1,1,1,1,1,1,1,1,1,1,1,1,1,1,1,1,1,1,1}

{1,1,1,1,1,1,1,1,1,1,1,1,1,1,1,1,1,1,1,1,1}

f=Interpolation[Transpose@{x,y}, InterpolationOrder→1]

InterpolatingFunction[{{-1.,1.}},<>]

Plot[f[t],{t,Min@x,Max@x},PlotRange→ {0,1},Filling→Axis]

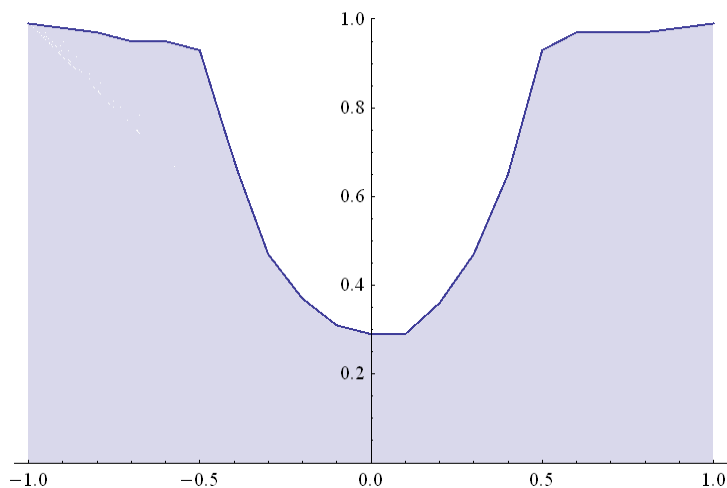
NIntegrate[f[t],{t,Min@x,Max@x},Method→"LocalAdaptive"]

1.679

2-1.679

0.321

JET 1

y1={0.99,0.98,0.97,0.97,0.97,0.93,0.65,0.47,0.36,0.29,0.29,0.31,0.37,0.47,0.68,0.93,0.95
,0.95,0.97,0.98,0.99}

{0.99,0.98,0.97,0.97,0.97,0.93,0.65,0.47,0.36,0.29,0.29,0.31,0.37,0.47,0.68,0.93,0.95,0.9
5,0.97,0.98,0.99}

f=Interpolation[Transpose@{x,y1}, InterpolationOrder→1]

InterpolatingFunction[{{-1.,1.}},<>]

Plot[f[t],{t,Min@x,Max@x},PlotRange→ {0,1},Filling→Axis]

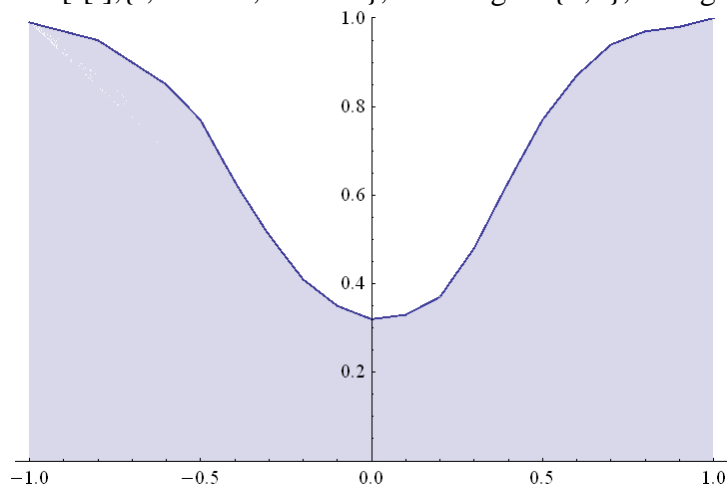NIntegrate[f[t],{t,Min@x,Max@x},Method→"LocalAdaptive"]

1.448

2-1.448

0.552

BASELINE

yb={1,0.98,0.97,0.94,0.87,0.77,0.63,0.48,0.37,0.33,0.32,0.35,0.41,0.51,0.63,0.77,0.85,0.9,0.95,0.97,0.99}

{1,0.98,0.97,0.94,0.87,0.77,0.63,0.48,0.37,0.33,0.32,0.35,0.41,0.51,0.63,0.77,0.85,0.9,0.95,0.97,0.99}

f=Interpolation[Transpose@{x,yb}, InterpolationOrder→1]

InterpolatingFunction[{{-1.,1.}},<>]

Plot[f[t],{t,Min@x,Max@x},PlotRange→ {0,1},Filling→Axis]

NIntegrate[f[t],{t,Min@x,Max@x},Method→"LocalAdaptive"]

1.3995

2-1.3995

0.600

Works Cited

[1] "Standard No. 111; Rearview Mirrors - Federal Motor Carrier Safety Administration." *Standard No. 111; Rearview Mirrors - Federal Motor Carrier Safety Administration*. Web. 3 Mar. 2014. <http://www.fmcsa.dot.gov/rules-regulations/administration/fmcsr/fmcsrruletext.aspx?reg=571.111>.

[2] "Sources." *EPA*. Environmental Protection Agency. Web. 2 Mar. 2014. <http://www.epa.gov/climatechange/ghgemissions/sources.html>.

[3] Hucho, I. "Aerodynamics of Road Vehicles." *Annual Review of Fluid Mechanics* 25.1 (1993): 485-537. Print.

[4] Zha,G.-C., "Low Noise and Low Drag Automobile Mirrors Using Jet Flow Control", UMM-115, University of Miami Invention Disclosure, Sept.7, 2012.

[5] Zha,G.-C., "Low Noise and Low Drag Automobile Mirrors," Provisional Patent files to USPTO, 61/765, 219,02/15/2013, 2013

[6] Zha,G.-C., "Low Noise and Low Drag Automobile Mirrors Using Jet Flow Control," Patent Cooperation Treaty, PCT/US2013/053191

[7] W.H. Hucho. Aerodynamik des Automobils, Wieweg Teubner, fifth edition, 2005

[8] Y,-Q. Shen and G.-C.Zha,"Large Eddy Simulation Using a New Set of Sixth Order Schemes for Compressible Viscous Terms," Journal of Computational Physics, vol229, pp.8296-8312,2010.

[9] "Separation of Boundary Layers." *Separation of Boundary Layers*. N.p., n.d. Web. 1 Mar. 2014.

[10] "Bernoulli Equation." *Pressure*. Web. 25 Mar. 2014. <http://hyperphysics.phy-astr.gsu.edu/hbase/pber.html>.

[11] Sudhakar, Y., and S. Vengadesan. "Vortex Shedding Characteristics of a Circular Cylinder with an Oscillating Wake Splitter Plate." *Computers & Fluids* 53 (2012): 40-52. Print.

[12] Perry, Mark J. "AEIdeas." *AEIdeas*. N.p., n.d. Web. 4 Mar. 2014.

[13] Im, H.-S., Zha, G.-C. and Dano, B., "Large Eddy Simulation of Co-Flow Jet Airfoil at High Angle of Attack", to appear in ASME Journal of Fluids Engineering, 2013

[14] Richardson, Lewis F. "Proceedings of the Royal Society of London. Series A, Containing Papers of a Mathematical and Physical Character." JSTOR. N.p., n.d. Web. 25 Mar. 2014.

[15] Baoyuan Wang, Ge-Cheng Zha, and Yiqing Shen "Detached-Eddy Simulations of a Circular Cylinder Using a Low Diffusion E-CUSP and High-Order WENO Scheme", AIAA Paper 2008-3855, AIAA 38th Fluid Dynamics Conference and Exhibit, 23 - 26 Jun 2008, Seattle, Washington

[16] Goodfellow, Sebastian D., Serhiy Yarusevych, and Pierre E. Sullivan. "Momentum Coefficient as a Parameter for Aerodynamic Flow Control with Synthetic Jets." *AIAA Journal* 51.3 (2013): 623-31. Print

[17] Zha, G.-C., Gao, W. and Paxton, C. D. "Jet Effects on Co-Flow Jet Airfoil Performance ", AIAA Journal, Vol.45, No.6, 2007, pp1222-1231

[18] Shen, Y.-Q. and Zha, G.-C., "Large Eddy Simulation Using a New Set of Sixth Order Schemes for Compressible Viscous Terms", Journal of Computational Physics, 2010, 229:8296-8312

[19] Im, H.-S., Zha, G.-C. and Dano, B., "Large Eddy Simulation of Co-Flow Jet Airfoil at High Angle of Attack", to appear in ASME Journal of Fluids Engineering, 2013

[20] Moreyra, Andres. Modified Low Noise and Low Drag Side Mirror. Thesis. University of Miami, 2014. N.p.: n.p., n.d. Print.